Oxygenated conditions in the aftermath of the Lomagundi-Jatuli Event: The carbon isotope and rare earth element signatures of the Paleoproterozoic Zaonega Formation, Russia

T. Kreitsmann[1*], A. Lepland[1,2,3], M. Bau[4], A. Prave[5], K. Paiste[1,2], K. Mänd[1,6], H. Sepp[1], T. Martma[7], A. E. Romashkin[8], K. Kirsimäe[1]

[1]Department of Geology, University of Tartu, 50411 Tartu, Estonia.

[2]CAGE—Centre for Arctic Gas Hydrate, Environment and Climate, Department of Geosciences, UiT The Arctic University of Norway, 9037 Tromsø, Norway.

[3]Geological Survey of Norway (NGU), 7491 Trondheim, Norway.

[4]Department of Physics and Earth Sciences, Jacobs University Bremen, Campus Ring 1, 28759 Bremen, Germany

[5]School of Earth and Environmental Sciences, University of St Andrews, St Andrews, KY16 9AL Scotland.

[6]Department of Earth & Atmospheric Sciences, University of Alberta, Edmonton, Alberta T6G 2E3, Canada.

[7]Department of Geology, Tallinn University of Technology, Ehitajate tee 5, 19086 Tallinn, Estonia

[8]Institute of Geology, Karelian Science Centre, Pushkinskaya 11, 185610 Petrozavodsk, Russia.

*Corresponding author: email timmu.kreitsmann@ut.ee

Abstract

The c. 2.0 Ga Zaonega Formation of the Onega Basin (NW Russia) has been central in efforts to understand what led to the initial rise (Great Oxidation Event, GOE) and postulated fall in free atmospheric oxygen and associated high-amplitude carbon cycle excursions, the Lomagundi-Jatuli Event (LJE) and subsequent Shunga Event during Paleoproterozoic time. The Formation accumulated shortly after the LJE and encompasses both the recovery in the carbon cycle and hypothesised contraction of the oceanic oxidant pool. However, interpreting the correct environmental context recorded by geochemical signatures in the Zaonega rocks is difficult due to a complex depositional and diagenetic history. In order to robustly constrain that history, we undertook a multiproxy study (mineralogy, petrography, carbon isotope and rare earth element composition) of carbonate beds in the upper part of the Zaonega Formation recovered in the 102-m composite section of the OnZap drill-cores. Our findings differentiate primary environmental signatures from secondary overprinting and show that: (i) the best-preserved carbonate beds define an upwards increasing $\delta^{13}C_{carb}$ trend from c. -5.4‰ to near 0‰; and that (ii) large intra-bed $\delta^{13}C_{carb}$ variations reflect varying contributions of methanotrophic dissolved inorganic carbon (DIC) to the basinal DIC pool. Rare earth element and yttrium (REY_{SN}) patterns confirm a marine origin of the carbonate beds whereas a consistent positive Eu_{SN} anomaly suggests a strong high temperature hydrothermal input during accumulation of the Zaonega Formation. Importantly, the presence of a negative Ce_{SN} anomaly in the REY_{SN} pattern indicates an oxygenated atmosphere-ocean system shortly after the LJE and indicates that models invoking a fall in oxygen at that time require reassessment.

Keywords: carbon isotopes, rare earth elements, Lomagundi-Jatuli Event, Ce anomaly, Zaonega Formationˇ

1. Introduction

Throughout most of Earth history the sedimentary carbonate carbon isotope record ($\delta^{13}C_{carb}$) has been relatively stable at around 0‰, reflecting an overall balance between carbon pools and sinks (Schidlowski, 2001). However, this trend is punctuated by several prominent excursions, one of the largest being the Lomagundi-Jatuli Event (LJE) at 2.22 – 2.06 Ga (Bekker and Holland, 2012; Karhu and Holland, 1996; Schidlowski et al., 1976). It followed and partly overlapped the Great Oxidation Event (GOE) and is characterised by the formation of ^{13}C-enriched carbonates with $\delta^{13}C_{carb}$ values reaching 15‰ (Bekker and Holland, 2012; Karhu and Holland, 1996). In several Paleoproterozoic basins, such as the Onega and Pechenga Basins in Fennoscandia and the Francevillian Basin in Gabon, the LJE-bearing carbonate rocks are overlain by rocks highly enriched in organic matter (commonly >10% TOC; Asael et al., 2013; Kump et al., 2011; Melezhik et al., 1999; Préat et al., 2011; Strauss et al., 2013); this remarkable burial of organic matter is known as the Shunga Event (SE; Strauss et al., 2013).

Both the LJE and SE are consequences of the dramatic changes in atmosphere-ocean chemistry and oxygenation that marked the Paleoproterozoic (Bekker and Holland, 2012; Holland, 2006; Kasting, 2001; Lyons et al., 2014). Different workers using datasets often derived from the same carbonate and organic-rich rock successions have arrived at varying to contradictory interpretations of the causal mechanisms that generated these perturbations of the carbon cycle. For the SE, some workers interpret Fe-speciation, C-, Mo- and S-isotope and trace element data as evidence that a global collapse in atmospheric oxygen occurred, leading to contraction of seawater sulfate levels and a worldwide ocean anoxia (Asael et al., 2013, 2018; Bekker and Holland, 2012; Canfield et al., 2013; Partin et al., 2013; Ossa Ossa et al., 2018; Planavsky et al., 2012; Scott et al., 2014). Others have put forward that weathering of organic-rich rocks under an oxygenated atmosphere resulted in a flux of isotopically light carbon into the world's oceans (Kump et al., 2011), with some workers pointing out that the

high concentration of redox-sensitive elements and elevated U isotope ratios in those rocks are indicative of prolonged elevated O_2 levels throughout SE time (Mänd et al., 2020; Sheen et al., 2018). Still others have used organic and carbonate carbon isotope and sulphur isotope signals to infer that the isotope perturbations in key SE successions are due to basin-specific, not global, conditions including diagenetic and hydrothermal overprinting and methanotrophy (Črne et al., 2014; Kreitsmann et al., 2019; Paiste et al., 2018; Qu et al., 2012, 2018).

Central to many of these studies have been the rocks of the Paleoproterozoic Onega Basin in NW Russia, specifically the Zaonega Formation recording the SE and the underlying Tulomozero Formation recording the LJE (Fig. 1; Melezhik et al., 2015). Here we report new stable carbon isotope, and rare earth element and yttrium (REY) data underpinned by detailed petrographic and mineralogical characterisation of carbonate rocks in the upper Zaonega Formation to study the paleoenvironmental and redox states of the atmosphere-ocean system spanning this intriguing interval of Earth history. Contrary to several studies that have inferred de-oxygenation in the upper Zaonega Formation, we find that carbonate rocks bearing post-LJE $\delta^{13}C$ signatures contain Ce anomalies suggestive of continuing ocean-atmospheric oxygenation.

2. Geological background

The Onega Basin consists of a volcanic and sedimentary succession formed between c. 2440 – 1890 Ma (Melezhik et al., 2015). The Zaonega Formation is in the upper part of that succession and contains the type locality – the village of Shunga – of the SE. Its lower part consists of rhythmically interbedded, fine-grained greywacke and mudstone and the upper part is organic-rich mudstone, siltstone, calcareous mudstone and dolostone (Črne et al., 2013, 2014). Contemporaneous with sedimentation was magmatic activity, as evidenced by lavas between

97 sedimentary packages and sills with peperite contacts (Črne et al., 2014; Qu et al., 2012). The
98 Zaonega Formation rests depositionally on the Tulomozero Formation which records the
99 positive $\delta^{13}C_{carb}$ excursion of the LJE (Brasier et al., 2011; Karhu, 1993) and is overlain by the
100 mafic and ultramafic lavas of the Suisari Formation. During the 1890 – 1790 Ma Svecofennian
101 orogeny, the succession experienced greenschist facies metamorphism (Melezhik et al., 1999).

102 Strongly positive $\delta^{13}C_{carb}$ values that typify the LJE occur in carbonate rocks in the
103 lower part of the Zaonega Formation (Melezhik et al., 2015) whereas the best-preserved $\delta^{13}C_{carb}$
104 values in the upper part of the Formation are at c. 0‰ (Črne et al., 2014; Kreitsmann et al.,
105 2019). This indicates that the Formation records the decline and termination of the LJE, which
106 in Fennoscandia occurred at 2.06 Ga (Karhu and Holland, 1996; Martin et al., 2013; Melezhik
107 et al., 2007) and provides a maximum age of deposition. The lower age limit is best constrained
108 by the 1988 ± 34 Ma age of a gabbro in the overlying Suisari Formation (Puchtel et al., 1999).
109 A U-Pb zircon age obtained by Martin et al. (2015) from a thin tuff bed (c. 5 cm thick)
110 interbedded with organic-rich mudstones in the lower to middle part of the Zaonega Formation
111 define a depositional age of 1982 ± 4.5 Ma.

112 The Zaonega Formation contains extremely organic-rich rocks (locally termed
113 shungite) with an average organic C content of c. 25% but reaching 98% in pyrobitumen veins
114 (Melezhik et al., 1999). $\delta^{13}C_{org}$ data define a profile in which values of c. -25‰ bracket an
115 excursion to as low as c. -40‰ in the middle and upper part of the Formation (Melezhik et al.,
116 1999; Paiste et al., 2018; Qu et al., 2012). Whether this accumulation of organic matter and the
117 associated $\delta^{13}C_{org}$ excursion were synchronous and global (Kump et al., 2011; Ossa Ossa et al.,
118 2018; Scott et al., 2014) or a consequence of temporally discrete basin-specific depositional
119 episodes (Lepland et al., 2014; Martin et al., 2015; Paiste et al., 2018; Qu et al., 2012, 2018)
120 remains debated.

3. Material and Methods

Samples were collected from dolostones and calcareous mudstones recovered in the OnZap1 (62.5870 N, 34.9310 E) and OnZap3 (62.5920 N, 34.9280 E) drill-cores from near the village of Shunga, Karelia, NW Russia (Fig. 1); they define a 102-m-thick composite section through the upper Zaonega Formation (for detailed information see Paiste et al., 2018). A total of 500 samples were taken for carbonate C and O isotope measurements by means of micro-drilling. Internal parts of carbonate beds were sampled at 10 cm spacing whereas sampling density increased to 2 to 5 cm approaching the bed contacts with the enclosing siliciclastic strata and cross-cutting silica veins.

Carbonate O and C stable isotope compositions of the samples were analysed using a Thermo Scientific Delta V Advance continuous flow isotope ratio mass spectrometer and a GasBench II preparation line connected to a Delta V Advantage IRMS (Thermo Fisher Scientific) at the University of Tartu and Tallinn University of Technology. The results of carbonate mineral analyses are expressed in *per mil* deviation relative to the Vienna PeeDee Belemnite (VPDB) scale for oxygen ($\delta^{18}O$) and carbon ($\delta^{13}C$). Long term reproducibility exceeded ±0.2‰ (2σ) for $\delta^{18}O$ and $\delta^{13}C$ values. The $\delta^{18}O$ values were corrected for the phosphoric acid fractionation factor for calcite and dolomite (Rosenbaum and Sheppard, 1986) in accordance with sample mineralogy.

Splits of micro-drilled samples were used for studying the mineralogical composition by means of X-ray diffractometry (XRD) at the University of Tartu. Unoriented preparations were scanned on a Bruker D8 Advance diffractometer using Cu *K*α radiation and LynxEye positive sensitive detector in 2–70° 2Θ range. Quantitative mineralogical composition was modelled using the Rietveld algorithm-based software, Topaz. The relative error of

quantification is better than 10% for major phases (>5 wt.%) and better than 20% for minor phases (<5 wt.%).

Thin sections and polished slabs of selected samples were studied using a ZEISS EVO MA15 scanning electron microscope (SEM). Chemical characterisation (point analyses and elemental mapping) was carried out with an Oxford AZTEC-MAX energy dispersive spectroscopy detector (EDS) attached to the SEM at the University of Tartu.

Twenty-nine micro-drilled samples were chosen for major and trace element analyses at Jacobs University Bremen. The samples were selected to span the entire OnZap section and to include different carbonate mineralogies. For analyses, 0.1 g of sample was measured and left to dry overnight at 105 °C. Dried samples were dissolved at high pressure at a temperature of c. 165 °C in an acid mixture of suprapure concentrated 3 ml HCl, 1 ml HNO_3 and 1 ml HF for 16 hours using a Picotrace digestion system. The acid-sample mixture was then evaporated twice by adding 5 ml suprapure concentrated HCl followed by additional dissolving in 0.5 M HNO_3. Major elements were measured with inductively coupled plasma optical emission spectrometry (ICP-OES) and trace elements with inductively coupled plasma mass spectrometry (ICP-MS). A dolomite standard reference material JDo-1 was used to monitor analytical quality. The REY concentrations were normalised against Post Archean Australian Shale (PAAS; Taylor and McLennan, 1985, except Dy from McLennan, 1989). The subscript "SN" denotes shale normalised values. Elemental anomalies were calculated in a linear method after Bau and Dulski, (1996) and Bolhar et al. (2004) and the bell-shape index (BSI) after Tostevin et al., (2016; Eq. 6) using the following equations:

$$(La/La^*)_{SN} = \frac{La_{SN}}{(3Pr_{SN} - 2Nd_{SN})} \qquad \text{(Eq. 1)}$$

$$(Ce/Ce^*)_{SN} = \frac{Ce_{SN}}{(0.5La_{SN} + 0.5Pr_{SN})} \qquad \text{(Eq. 2)}$$

$$(Pr/Pr^*)_{SN} = \frac{Pr_{SN}}{(0.5Ce_{SN}+0.5Nd_{SN})} \quad \text{(Eq. 3)}$$

$$(Gd/Gd^*)_{SN} = \frac{Gd_{SN}}{(2Tb_{SN}+Dy_{SN})} \quad \text{(Eq. 4)}$$

$$(Eu/Eu^*)_{SN} = \frac{Eu_{SN}}{(0.67Sm_{SN}+0.33Tb_{SN})} \quad \text{(Eq. 5)}$$

$$BSI = \frac{2*(Sm_{SN}+Gd_{SN}+Dy_{SN})/3}{(La_{SN}+Pr_{SN}+Nd_{SN})/3 + (Ho_{SN}+Er_{SN}+Tm_{SN}+Yb_{SN}+Lu_{SN})/5} \quad \text{(Eq. 6)}$$

4. Results

4.1. Mineralogy and petrography

As defined in Paiste et al. (2018), we adopt the division of the OnZap section into three units: Unit A from depth 102 to 53 m is composed of black organic-rich mudstone, calcareous mudstone and dolostone; Unit B from depth 53 – 33 m consists of dolostone interlayered with organic-rich mudstone; and Unit C from 33 – 1.7 m depth is characterised by grey, organic-poor mudstone and marl (Fig. 2). In total, the OnZap section contains 11 carbonate-bearing intervals that have distinct geochemical patterns, mineralogy and petrography (Table 1).

Unit A has five carbonate intervals. A5 is dolomitic (dolomite content up to 89.5 wt.%), A2 and A3 are calcitic (up to 75.7 wt.%) and A1 and A4 have mixed carbonate mineralogy. Dolomite is characterised by fine-grained aggregates, 20 – 40 μm in size, of planar-s crystallites with minor Fe (Fig. 3A and B). In A5 dolospar is present as planar-s to nonplanar locally zoned crystallites 200 – 300 μm in size that have undergone dedolomitisation (Fig. 3C). Calcite occurs in three forms: (i) fine-grained (<100 μm in diameter) euhedral crystals (Fig. 3D); (ii) macroscopically visible poikilitic aggregates that have many inclusions of host-rock minerals (Fig. 3E); (iii) masses of anhedral calcite replacing dolomite (Fig. 3C, F). The calcareous

188 mudstones in Unit A contain significant amounts of micas, quartz, feldspar and talc (Fig. 2,
189 Supplementary Table 1).

190 In Unit B, there are three carbonate intervals. B1 is marked by massive dolospar beds
191 interlayered with organic-rich mudstones and is associated with secondary hydrothermal
192 silicification. The internal parts of the beds consist of relatively pure dolomite (up to 94.8 wt.%)
193 but calcite content increases towards bed margins to as high as 83.5 wt.% (Fig. 2, Table 1). B2
194 is a calcareous mudstone with calcite occurring in three forms: small (20 – 40 μm) subhedral
195 crystals with mica rims and some with quartz grain cores; large (>1 mm) calcite crystals as
196 early formed aggregates (laminae are compacted around the aggregates); or calcite aggregates
197 that cross-cut laminae and contain mica. Interestingly, some of the calcite is well-rounded
198 suggesting that it was reworked and transported as a sedimentary particle. B3 is also marked
199 by massive dolomite but with less secondary hydrothermal alteration. Dolomite textures in Unit
200 B vary from planar-e (Fig. 4A) and planar-s (Fig. 4B) to nonplanar crystals including, in rare
201 cases, void-filling dolomite crystals (Fig. 4C). Dolomite crystals are between 200 – 400 μm in
202 size, zoning is rare and Fe content does not vary as much as in the other units. Calcite in B1
203 and B3 intervals form large anhedral aggregates that replace and/or surround dolomite (Fig.
204 4D).

205 Three carbonate intervals occur in Unit C, all of which contain abundant Fe-rich
206 ankerite-dolomite solid-solution minerals (Fig. 5 and 6) characterised by planar-e to planar-s
207 zoned rhombohedral crystals (Fig. 5A, B and C) marked by varying Mg, Fe and, to lesser
208 extent, Mn concentrations (Fig. 5C). Calcite is rare and does not exceed 12 wt.%. C1 contains
209 secondary Fe-rich dolomite aggregates with crystals 20 – 40 μm in size. C3 has also siderite,
210 up to a concentration of 7.6 wt.% (Supplementary table 1). Siderite occurs as anhedral
211 aggregates, ~0.5 mm in size, commonly surrounded by pyrite, and many aggregates contain
212 inclusions of partially dissolved dolomite rhombs (Fig. 5D). Unlike Units A and B in which

carbonate cement is mostly calcite, Unit C is marked by an Fe-rich dolomitic cement and the concentration of Fe increases upward from C1 to C3.

4.2. Carbonate $\delta^{13}C$ and $\delta^{18}O$ isotopes

Although carbonate $\delta^{13}C$ and $\delta^{18}O$ values exhibit large variation (Fig. 2, Supplementary Table 1), the overall trend is one in which both increase upward through the Zaonega Formation and then decline slightly in the uppermost strata. In most instances, higher $\delta^{13}C_{carb}$ values occur in the interior parts of carbonate beds and decrease toward bed margins; in B1 and to some extent in A4 and A5 this change is also accompanied by increasing calcite abundance. The exceptions to this pattern are A1 and A2, where $\delta^{13}C_{carb}$ values increase towards the bed margins (Fig. 7), and A3, where values remain relatively constant around -10.2 ± 1.0‰.

In Unit A, $\delta^{13}C_{carb}$ and $\delta^{18}O$ values for dolomite-rich (calcite wt.% tototal carbonate wt.% ratio <0.2) samples range between -13.9‰ and -6.0‰, and -13.8‰ and -11.2‰, respectively (Fig. 8). For calcite-rich (calcite wt.% to total carbonate wt.% ratio >0.8) samples, $\delta^{13}C_{carb}$ and $\delta^{18}O$ values are between -25.3‰ and -8.6‰ and -14.7‰ and -10.4‰, respectively (Fig. 8).

In Unit B, isotope values also show large variability but, in general, $\delta^{13}C_{carb}$ increases from -12.8‰ to -1.0‰ in B1, decreases back to -16.4‰ in the calcareous mudstones of B2 and then increases to near 0‰ in B3 (Fig 2). The $\delta^{13}C_{carb}$ and $\delta^{18}O$ values in dolomite-rich samples are between -12.6‰ and -0.9‰ (outliers as low as -18.9‰), and -14.7‰ to -8.6‰ (outliers as high as -5.2‰), respectively. In calcite-rich samples, $\delta^{13}C_{carb}$ and $\delta^{18}O$ values vary between -16.4‰ and -6.3‰, and -14.0‰ and -12.5‰ (one outlier at -10.6‰), respectively (Fig. 8).

The C1 interval exhibits variable $\delta^{13}C_{carb}$ and $\delta^{18}O$ values between -11.3‰ and +0.8‰, and -11.1‰ and -5.8‰, respectively. In C2, $\delta^{13}C_{carb}$ values decrease from -2.9‰ to -6.2‰ and $\delta^{18}O$ values from -10.9‰ to -13.4‰ towards the top of C3 (Fig. 2).

4.3. Major and trace elements

Major and trace element concentrations are shown in Supplementary Table 2. In Unit A, Fe content varies between 0.3 and 3.6 wt.%, in Unit B between 0.06 and 1.1 wt.% and in Unit C between 4.8 and 6.1 wt.%. Manganese content shows a similar trend as Fe, with the lowest concentrations in Unit B and the highest in Unit C: 0.05 to 0.13 wt.% and 0.32 to 0.68 wt.%, respectively. In Unit A, Mn concentrations are between 0.09 and 0.3 wt.%.

Each unit has distinctive REY_{SN} patterns (Supplementary Table 3). In Unit A (n=13), the total REE (ΣREE) concentrations range between 19.19 and 159.16 ppm (mean 46.79 ± 40.05 ppm). Y/Ho ratios are slightly above the chondritic ratio of 27 and range from 29.09 to 37.32 (mean 33.46 ± 2.63), whereas La_{SN} anomalies $[(La/La^{*})_{SN}]$ are typically positive from 0.92 to 1.73 (mean 1.42 ± 0.29, excluding two outliers -13.62 and 12.15). Further, there is a positive Gd_{SN} anomaly $[(Gd/Gd^{*})_{SN}$: 1.08 - 1.3; mean 1.20 ± 0.07] and light REE (LREE; La to Nd) are depleted compared to heavy REE (HREE; Ho to Lu) as shown by Pr_{SN}/Yb_{SN} ratios between 0.09 and 1.15 (mean 0.45 ± 0.31). In contrast, middle REE (MREE; Sm to Dy) are enriched compared to LREE and HREE with BSI varying from 0.97 to 1.69 (mean 1.41 ± 0.22). There is a strong positive Eu_{SN} anomaly $[(Eu/Eu^{*})_{SN}$: 1.17 - 3.21; mean 1.79 ± 0.5]. $(Ce/Ce^{*})_{SN}$ values vary from 0.58 to 0.89 (mean 0.75 ± 0.1) with $(Pr/Pr^{*})_{SN}$ ranging between 0.99 and 1.1 (mean 1.04 ± 0.04). Immobile trace elements Sc, Zr and Th show varying concentrations from 1.2 to 6.8 ppm, 2.05 to 39.04 ppm, and 0.09 to 2.84 ppm, respectively.

In Unit B (n=12), ΣREE values range from 4.44 to 41.17 ppm (mean 16.27 ± 11.51 ppm) and Y/Ho ratios are higher than in Units A and C (Y/Ho: 32.98 – 49.63; mean 39.01 ± 4.28). Unit B shows positive La_{SN} and Gd_{SN} anomalies between 1.16 and 1.70 (mean 1.41 ± 0.15) and 1.20 and 1.37 (mean 1.27 ± 0.05), respectively. LREE are depleted compared to HREE with $(Pr/Yb)_{SN}$ ratios from 0.09 to 0.60 (mean 0.32 ± 0.14). Unit B does not show any

significant MREE enrichment and BSI values range between 0.92 – 1.22 (mean 1.04 ± 0.1). Compared to other units there is a smaller but still positive Eu_{SN} anomaly, from 0.82 to 2.40 (mean 1.65 ± 0.52), $(Ce/Ce^*)_{SN}$ values show the largest negative anomaly, varying between 0.40 and 0.91 (mean 0.68 ± 0.13) and $(Pr/Pr^*)_{SN}$ varies between 0.99 – 1.36 (mean 1.11 ± 0.1). Unit B also has the lowest Sc, Zr and Th concentrations: 0.27 – 2.16, 0.78 – 22.26, and 0.05 – 0.34 ppm, respectively.

Given that Unit C is dominated by shales, only four carbonate samples were chosen for trace element analyses, and most of those showed a strong contribution from the siliciclastic fraction as indicated by high Sc, Zr and Th concentrations with some samples having 12.45, 110.97, and 3.51 ppm, respectively. ΣREE ranges from 11.74 to 69.14 ppm (mean 33.35 ± 22.13 ppm), Y/Ho ratios are from 23.92 to 33.73 (mean 28.86 ± 3.53, hence close to the chondritic value), $(La/La^*)_{SN}$ varies between 0.88 and 1.38 (mean 1.07 ± 0.2), $(Gd/Gd^*)_{SN}$ is between 1.09 and 1.18 (mean 1.13 ± 0.03) and there is a small LREE depletion with $(Pr/Yb)_{SN}$ varying between 0.41 and 0.88 (mean 0.69 ± 0.18). Unit C shows the highest MREE enrichment with BSI from 1.18 to 2.03 (mean 1.57 ± 0.33) and positive Eu_{SN} anomalies with $(Eu/Eu^*)_{SN}$ ranging from 1.30 to 2.66 (mean 1.95 ± 0.5). Ce does not show anomalous behaviour: $(Ce/Ce^*)_{SN}$ ranges between 0.93 and 1.02 (mean 0.98 ± 0.03) and $(Pr/Pr^*)_{SN}$ from 0.97 to 1.03 (mean 1.0 ± 0.03).

4.4. Preservation of the $\delta^{13}C_{carb}$ signal

The organic-rich siliciclastic-carbonate sediments of the Zaonega Formation were deposited in a volcanically active basin and experienced complex post-depositional overprinting processes resulting in a heterogeneous mineralogy (Črne et al., 2014; Kreitsmann et al., 2019; Melezhik et al., 2015). Jacobsen and Kaufman (1999) have shown that carbon isotopes can be altered if the water-rock ratio is very high such that carbon and oxygen isotope values will define an L-

shape declining curve. The C- and O-isotope ratios in OnZap section define such a curve (Fig. 9), implying that they experienced secondary alteration and that screening of the samples is necessary in order to extract information about the depositional environment

The Mn/Sr_{carb} ratio is commonly used to assess the effect of meteoric alteration in marine carbonates (Brand and Veizer, 1980). For example, a Mn/Sr_{carb} ratio <10 has previously been used as a screening tool for Proterozoic rocks (Kaufman and Knoll, 1995; Melezhik et al., 2015). However, Kreitsmann et al. (2019), in their study of rocks correlative to the OnZap section in the OPH drill core, have shown that the Mn/Sr_{carb} ratio <10 criterion is not always a reliable indicator of better preserved samples and additional, thorough petrographic and mineralogical characterisation are necessary. In the OPH core, as well as in the FAR-DEEP 12AB, 13A (Črne et al., 2014) and OnZap drill cores, calcitic margins (dedolomite) have formed on carbonate beds with $\delta^{13}C_{carb}$ values as much as 15‰ lower than those in the better preserved dolomite interiors. Yet, the Mn/Sr_{carb} ratio is lower in the dedolomite than in the original dolomite (Kreitsmann et al., 2019). Hence, in rocks with a mixed carbonate mineralogy, the Mn/Sr_{carb} ratio may not be a robust screening tool because calcite incorporates Sr preferentially, whereas dolomite does so with Mn (Veizer, 1983). Furthermore, the Mn/Sr_{carb} filter was developed for use in the context of freshwater alteration in Phanerozoic environments (Brand and Veizer, 1980); chemistry of such environments in the lower-O_2 Proterozoic is likely to have been markedly different. In the case of the OnZap samples, our analyses obtained average Mn/Sr_{carb} values of 9.02 ± 7.25 and 7.53 ± 4.4 for Units A and B, respectively, whereas Unit C, containing mostly Fe-rich ankerite-dolomite with only minor calcite, has an Mn/Sr_{carb} average of 53.91 ± 38.5. While some of this contrast might result from varying degrees of overprinting, it more likely that tracks a different depositional environment in Unit C leading to different mineralogy compared to Units A and B.

309 Here we have, instead, opted for a combined mineralogical and oxygen isotope
310 approach for sample screening. In studies that have combined high-resolution geochemical and
311 isotope analyses with careful petrography and detailed mineralogy (e.g., Črne et al., 2014;
312 Kreitsmann et al., 2019), the emerging picture is that calcite in the upper Zaonega Formation
313 is largely a secondary carbonate phase, whereas dolomite is primary, except the calcareous
314 mudstone bed A2 which will be discussed separately. Further, there is mostly complete
315 resetting of isotopic signals at bed margins but bed interiors retain a better preserved, likely
316 original, carbon isotope signal. Consequently, we use a calcite to total carbonate ratio <0.05 as
317 a cut-off value to screen for the better-preserved samples with a primary carbon isotope signal
318 (Fig. 10). We combine this with a $\delta^{18}O$-based screen using a $\delta^{18}O$ cut-off value >-10.0‰. On
319 the $\delta^{18}O$ and $\delta^{13}C_{carb}$ cross-plot (Fig. 9), there is no obvious correlation in samples having $\delta^{18}O$
320 values >-10.0‰, indicating that carbon isotopes in these samples carry a better-preserved
321 signal (Derry, 2010).

322 **4.5. Contamination in the carbonate REY_{SN} signal**

323 In order to use the carbonate REY_{SN} signal as a paleoenvironmental indicator, samples must
324 be screened to eliminate those with contamination from siliciclastic detritus, Fe-Mn oxides,
325 sulphides and phosphates (Bau, 1993; Kamber et al., 2014; Wang et al., 2018), all of which
326 carry considerably higher concentrations of REY compared to pure carbonates. The extent of
327 siliciclastic contamination is commonly monitored using the concentration of immobile trace
328 elements (e.g., Zr and Th; Bau, 1993; Bolhar and Van Kranendonk, 2007; Frimmel, 2009;
329 Kamber et al., 2014; Schier et al., 2018; Viehmann et al., 2015a, 2015b; Zhao and Zheng, 2017)
330 and by observing whether these elements correlate with typical seawater features such as
331 positive La_{SN} anomalies and supra-chondritic Y/Ho ratios (Schier et al., 2018; Viehmann et al.,
332 2015b, 2015a; Wang et al., 2018). Siderophile Ni and Cu can be monitored for contamination
333 by oxides and chalcophile Pb and Sc for contamination by sulphides (Fig. 11; Bolhar and Van

Kranendonk, 2007). X-ray diffraction can be used to monitor the contribution of phosphate to the carbonate REY_{SN} pattern. Lastly, carbonate rocks typically have low REE concentrations; thus, if contaminated, their ΣREE concentration would increase and in a binary plot of immobile trace elements to ΣREE concentration show a positive correlation.

We used a Zr concentration of <4 ppm (as suggested by Frimmel, 2009) as the cut-off value to screen carbonate samples for terrigenous contamination. For phosphate, our XRD data show that apatite does not exceed 1.2 wt.% (usually <1 wt.%) in the screened samples (in fact, the sample with the highest apatite abundance has the lowest ΣREE concentration; Supplementary Table 3). Nine dolomite samples passed our screening: one sample each from A5, B3 and C2 and six samples from B1 (Fig. 11; Supplementary Table 3). None of the dedolomitised samples passed. These 9 samples retained their original REY signal and can be used as reliable archives of paleoenvironmental proxies.

5. Discussion

The Zaonega Formation has figured prominently in recent efforts to better understand the oxygenation state of the Paleoproterozoic Earth system but, as highlighted in the Introduction, these efforts have come to contradicting conclusions: either global contraction of oxygen levels (Asael et al., 2013, 2018; Kipp et al., 2017; Scott et al., 2014); elevated oxygen levels during deposition of the Zaonega Formation (Mänd et al. 2020; Sheen et al., 2018) or fluctuating basinal redox conditions (Paiste et al., 2018). Hence, views are divergent on the oxygenation state of the Paleoproteorzoic atmosphere-ocean system following the LJE. Below, we summarise and discuss our C-isotope and REY data; the latter in particular provides an independent proxy with the potential to resolve these divergent scenarios.

5.1. Variations within individual intervals and stratigraphic $\delta^{13}C_{carb}$ trend in the OnZap section

Carbonate beds in intervals A1 and A2 have a distinctive reverse $\delta^{13}C_{carb}$ pattern compared to other carbonate beds as the $\delta^{13}C_{carb}$ values become increasingly higher towards the margins of the beds ($\delta^{13}C_{carb}$ values -15‰ in A2 and -10‰ in A1) compared to the interior parts that have values as low as -25‰ (Fig. 7). As we and other workers (Črne et al., 2014; Kreitsmann et al., 2019; Paiste et al., 2018) have documented through detailed bed-by-bed study of the Zaonega rocks, bed margins are affected by secondary processes whereas bed interiors house the best-preserved isotope signals. Thus, the $\delta^{13}C_{carb}$ values of -15‰ to -10‰ are observed at all bed margins throughout Unit A and B, like those elsewhere, a consequence of hydrothermal alteration. Accordingly, as per beds elsewhere, the isotopically lighter carbonates within bed interiors in intervals A1 and A2 record a pre-alteration signal. The $\delta^{18}O$ values of intervals A1 and A2 are, in contrast, relatively uniform and do not exhibit a difference between the interiors and margins, possibly reflecting a wholesale oxygen isotope resetting during the hydrothermal alteration. Further, the upper strata of the Zaonega formation contain a record of ubiquitous syndepositional methane cycling and methanotrophy (Qu et al., 2012, 2018). Thus, we suggest that the low $\delta^{13}C_{carb}$ values in the interiors of carbonate intervals A1 and A2 evidence for early-diagenetic methane derived carbonates formed *via* anaerobic oxidation of methane (AOM) in an ancient seep system.

AOM derived carbonates are widely observed in modern hydrocarbon seeps but examples can be also found in the Precambrian (Campbell, 2006). The ^{13}C-depleted carbon source for the precipitation of authigenic seep carbonates is supplied by microbially mediated anaerobic oxidation of hydrocarbons such as methane and oil (Boetius et al., 2000; Joye et al., 2010), typically within shallow subsurface sediments. In these settings, hydrocarbons rising through unconsolidated sediments are anaerobically oxidised at the lower boundary of the

sulfate reduction zone by microbial consortia of methanotrophic archaea and sulfate-reducing bacteria (Boetius et al., 2000; Orphan et al., 2002; Whiticar, 1999). Anaerobic oxidation of methane increases pore-water alkalinity and consequently causes the precipitation of carbonates with ^{13}C-depleted signatures whose values depend on the origin of the methane. Biogenic methane produced by methanogens is strongly depleted in ^{13}C and its $\delta^{13}C$ values vary from -110 to -50‰, typically -60 ± 5‰ (Sapart et al., 2012; Schoell, 1988). Thermogenic methane typically has higher $\delta^{13}C$ values, from lower than -50‰ up to -22 ± 3‰ in pyrogenic methane (Sapart et al., 2012), that become increasingly heavier with increasing maturity of organic matter (Whiticar, 1999).

Given hydrocarbon generation and circulation, triggered by magmatic activity during accumulation of the middle and upper Zaonega succession (Qu et al., 2012), precipitation of AOM-derived carbonates is expected to occur in a similar manner as that observed in the late Paleocene Vøring Basin (Norwegian Sea; Svensen et al., 2003) or in the modern seeps of the Guaymas Basin in the Gulf of California (Geilert et al., 2018; Simoneit et al., 1990) where hydrothermal systems initiated by magmatic activity produce seep carbonates. Usually the AOM-derived carbonates that consume microbial methane have $\delta^{13}C_{carb}$ values <-30‰ (Campbell, 2006); however, the isotope composition of the carbonate precipitating in the system is a mixed signal strongly influenced by the relative balance between DIC derived from AOM and seawater (Himmler et al., 2010). Alternatively, variation in the source of methane, i.e., microbial versus thermogenic origin can also produce methane-derived carbonates of variable $\delta^{13}C$. Slightly higher $\delta^{13}C_{carb}$ values in the OnZap carbonate intervals A1 and A2 compared to common methane derived carbonates can, thus, be explained by mixing with the seawater DIC pool and/or by thermogenic CH_4 being the dominant source. The AOM derived origin of A1 and A2 carbonates is further evident by the presence of likely barite pseudomorphs (Fig. 3H). Barite is a common precipitate at sulfate–methane interfaces in

methane/hydrocarbon seeps where ascending fluids from anoxic sediments containing methane and Ba^{2+} (leached from K-minerals) interact with sulfate near the AOM zone (Castellini et al., 2006; Griffith and Paytan, 2012).

Alternatively, the isotopically light interiors of intervals A1 and A2 could represent carbonate concretions formed as a result of an alkalinity boost due to organoclastic sulfate reduction in the diagenetic realm (Irwin et al., 1977). The carbon isotope values in diagenetic carbonate concretions can be variable (from -43‰ to +13‰), with a significant overlap with different organic matter mineralization reactions (e.g., sulfate reduction, methanogenesis and thermal decarboxylation; Raiswell and Fisher, 2000). Given the abundance of biomass and its $\delta^{13}C$ values around -35‰, it is possible that strongly ^{13}C-depleted porewater DIC generated through mineralization of organic matter was responsible for the precipitation of these low-$\delta^{13}C$ carbonates.

Moving upsection, the petrography of A3 calcareous mudstone resembles the A1 and A2 intervals (e.g., calcite cement). However, the $\delta^{13}C_{carb}$ values of A3 are relatively stable (c. -10.2 ± 1‰) with similar values to the outer edges of A1 and A2 intervals that might reflect the resetting of initial AOM signals as in A3. Likewise, varying dolomite/calcite ratios and carbon isotopic signals of the calcareous mudstone interval A4 suggests that most of the original signal has been overprinted by intensive dedolomitisation and/or recycling of organic matter. Depending on the relative concentration of bicarbonate produced *via* microbial oxidation of OM relative to the total amount of carbon in the system, organic diagenesis can decrease or increase (e.g., through methanogenesis) the $\delta^{13}C_{carb}$ values of carbonate rocks (Irwin et al., 1977; Mazzullo, 2000; Swart, 2015). In contrast, the purer and less organic-rich dolostone intervals in the upper part of Unit A through Unit C must have been less influenced by organic diagenesis than the organic-rich calcareous mudstones of Unit A. Like the calcareous mudstone interval A4, dolostone intervals A5 and B1 did, however, experience

dedolomitisation at contacts between carbonate beds and mudstones, which resulted in lower isotopic values on the margins compared to interiors of carbonate beds. Intra-bed $\delta^{13}C_{carb}$ variation (more than 5‰; Fig. 10) is probably due to the varying influence of methanotrophic bicarbonate to the DIC pool of ambient seawater and/or organic diagenesis.

In the calcareous mudstone interval B2 the $\delta^{13}C_{carb}$ values vary between -16.4‰ and -12.8‰; upsection, through intervals B3 and C1values shift to +0.8‰. This excursion also coincides with a transition from methanotrophy-contributed biomass ($\delta^{13}C_{org}$ values of -40 to -35‰) to predominantly phototrophic biomass ($\delta^{13}C_{org}$ values of -25‰; Fig. 2; Paiste et al., 2018). In addition, most of Unit C's Mn/Sr_{carb} ratios, REY_{SN} patterns, petrography and mineralogy differs notably from the other units. Dolomite in Unit C rocks is typically zoned and becomes increasingly more Fe-rich towards the top of the succession, as the carbonate composition changes from dolomite to ankerite with siderite aggregates (Fig. 6). Petrography and carbon isotopes suggest that dolomite in Unit C, except for the first two meters of C1, is diagenetic and precipitated from Fe-rich anoxic pore-waters. There are no signs of significant secondary alteration. In that regard our data agree with Paiste et al. (2018) who concluded that the thick dolomite bed in Unit B acted as a stratigraphic seal that hindered further ascent of dedolomitising hydrothermal fluids.

5.2. The secular $\delta^{13}C_{carb}$ trend of the upper Zaonega Formation

Screening of carbonate isotope data for the OnZap succession based on petrographical, mineralogical and chemical criteria shows that, similar to the upper part of the Zaonega Formation in FAR-DEEP 13A, 12AB and OPH drill-cores, the least-altered carbonate samples are in the middle parts of carbonate beds (Črne et al., 2014; Melezhik et al., 2015, Kreitsmann et al., 2019). None of the samples from Unit A passed the mineralogical and $\delta^{18}O$ screening. The screened $\delta^{13}C_{carb}$ values in Unit B (n=29) vary from -5.4‰ to -0.9‰ and shift to more

positive values towards the top of Unit B (Fig. 10). The same $\delta^{13}C_{carb}$ trend continues in the lower part of Unit C (n=8) with $\delta^{13}C_{carb}$ values increasing from -3.8‰ to 0.83‰, although most of Unit C is represented by diagenetic carbonates.

Confirming what has been found in earlier studies (e.g., Črne et al., 2014; Melezhik et al., 2015), this study reveals a negative excursion following the LJE in the upper Zaonega Formation. The $\delta^{13}C_{carb}$ values as low as c. -20‰ in the middle and upper part of the Zaonega Formation are now known to be due, in part, to diagenetic and hydrothermal processes (Črne et al., 2014; Kreitsmann et al., 2019). Our screened samples for the upper Zaonega Formation, which have values between -5.4‰ and +0.8‰, offer a better-preserved record of ocean chemistry at the time of deposition. A similar transition in $\delta^{13}C_{carb}$ values in the lower part of the upper Zaonega Formation in FAR-DEEP and OPH cores, i.e. from -6 to -2‰ and -6 to 0.5‰, respectively, has been described by other workers (Črne et al., 2014; Melezhik et al., 2015; Kreitsmann et al., 2019). Such analogous behaviour of $\delta^{13}C_{carb}$ in correlative successions at three different localities suggest a basin-wide nature of this trend. Nevertheless, variable scattering of intra-bed $\delta^{13}C_{carb}$ values in the OnZap cores, and also in correlative intervals of the OPH (Kreitsmann et al., 2019) and FAR-DEEP cores (Črne et al., 2014), suggests large lateral/local isotopic variability of the DIC pool in the Onega Basin during accumulation of the Zaonega Formation. We suggest that this variability reflects proximity of a particular area of carbonate precipitation to active methane seeps and, hence, methane influence into the DIC pool and carbonate $\delta^{13}C_{carb}$. This suggests that the negative excursion in the Onega Basin can be related to basin-specific processes and cannot be used to infer the isotopic composition of the global seawater DIC pool until similar negative excursions with the same extent are identified in other post-LJE successions.

5.3. Paleoenvironment in the aftermath of the LJE in the Onega Basin

Abundances of the lanthanides and yttrium in sedimentary precipitates (e.g., cherts, phosphates, carbonates) can be used as a proxy for ancient seawater compositions and redox states (Alexander et al., 2008; Allwood et al., 2010; Bau and Alexander, 2006; Bellefroid et al., 2019; Kamber et al., 2014; Kamber and Webb, 2001; Schier et al., 2018; Shields and Stille, 2001). In modern seawater, the REY signal is largely dominated by products of continental weathering and dust. Input by hydrothermal activity at the ocean floor is insignificant in modern systems but was more pronounced during the Archean, as evidenced by the widespread positive Eu_{SN} anomalies in Archean chemical sediments (Alexander et al., 2009; Bau and Dulski, 1996; Viehmann et al., 2015b).

REY speciation in seawater is influenced by two competing processes: stronger complexation between dissolved ligands (e.g., CO_3^{2-}) and HREE as well as preferential adsorption of LREE on settling particles (Elderfield, 1988), which result in progressive enrichment of HREE compared to LREE and MREE in seawater REY_{SN} patterns. Seawater is also characterised by positive La_{SN}, Gd_{SN} and possibly Lu_{SN} anomalies (Bau and Dulski, 1999; Bolhar et al., 2004; Tostevin et al., 2016) and decoupling of Y and Ho due to preferential adsorption of Ho on Fe-Mn-particles compared to Y (Bau et al., 1996; Nozaki et al., 1997). As a consequence, the Y/Ho ratio becomes super-chondritic (>44) in open-marine settings, whereas <44 are expected in restricted environments or those with freshwater and strong hydrothermal influence (Bau et al., 1995; Bolhar and Van Kranendonk, 2007; Kamber and Webb, 2001; Nozaki et al., 1997). Positive La_{SN} and Gd_{SN} anomalies, super-chondritic Y/Ho ratios, LREE depletion compared to HREE and uniform REY_{SN} data in screened samples of OnZap section (Fig. 12D; Supplementary Table 3) all suggest that samples from Unit B carry the REY signature of ambient seawater. This also agrees with carbon isotopes that carry near-normal marine $\delta^{13}C_{carb}$ values in Unit B.

505 A positive Eu_{SN} anomaly is present in all the screened samples, ranging between 1.24
506 and 2.26 (Fig. 12). Europium can be decoupled from other trivalent REE in high-temperature
507 hydrothermal fluids (>250 °C) where Eu^{3+} is reduced to Eu^{2+} (Bau, 1991; Sverjensky, 1984).
508 The latter has a strong affinity to Cl^- complexation and more readily accumulates in solution,
509 whereas Eu^{+3} behaves similarly to other trivalent REE (Douville et al., 1999). As temperature
510 drops due to conductive cooling or mixing with ambient seawater, Eu^{2+} is re-oxidised, but the
511 excess Eu persists and is transferred to inorganic and biogenic precipitates such as sedimentary
512 and biogenic carbonates (e.g., Bau et al., 2010; Merschel and Bau, 2015). In very Ba-rich
513 samples positive Eu_{SN} anomalies can be analytical artefacts because of overlap of the masses
514 of BaO and Eu in ICP-MS analyses. However, in our samples there is no correlation between
515 measured Eu and Ba concentrations and at the low Ba/Eu ratios of these samples the correction
516 procedure for the isobaric BaO intrerference on Eu, which is based on experimentally
517 determined BaO yields in matrix-matched solutions, is not compromised. Noteworthy is that
518 the negative Ce_{SN} anomalies and well-preserved C isotopes of the screened samples eliminate
519 the possibility that the REY data reflect post-depositional overprinting.

520 While positive Eu_{SN} anomalies are common in Archean carbonates (Allwood et al.,
521 2010; Kamber and Webb, 2001; Schier et al., 2018), they are very rare in Proterozoic marine
522 carbonates (Bau and Alexander, 2006; Schier et al., 2018; Wang et al., 2018), suggesting a
523 diminishing influence of high-temperature hydrothermal input as a source of REY. This is
524 strongly supported by Nd isotope data for Precambrian marine chemical sediments such as
525 carbonates and banded iron-formations, that suggest a decreasing flux of hydrothermally-
526 sourced mantle Nd relative to continental Nd into seawater (e.g., Viehmann et al., 2015a; Schier
527 et al., 2018). If the selective Eu enrichment in Paleoproterozoic seawater was a global feature,
528 which is suggested by published data, the presence of prominent Eu_{SN} anomalies in the studied
529 samples implies that the Zaonega sediments were deposited in a semi-restricted basin, as in an

open-marine setting the excess Eu would be rapidly diluted. This interpretation agrees with the geological context of the Zaonega Formation, which was marked by significant syndepositional volcanic and hydrothermal activity (e.g., Črne et al., 2014) as well as basinal restriction during its deposition suggested by Paiste et al. (2018; 2020).

The redox status of seawater during the formation of modern and ancient carbonates has been widely assessed using Ce behaviour (Bellefroid et al., 2018; Elderfield and Greaves, 1982; Liu et al., 2019; Tostevin et al., 2016; Webb and Kamber, 2000; Wright et al., 1987). In modern oxic seawater, dissolved Ce^{3+} is oxidised to more particle-reactive Ce^{4+} oxide on the surface of Fe-Mn-(hydr)oxides and is removed from seawater by deposition of particulate and colloidal material (Bau and Koschinsky, 2009). As a result, modern seawater shows a distinctive negative Ce_{SN}-anomaly. However, a Ce_{SN} anomaly does not necessarily describe the redox-conditions in the water column at the depositional site. Negative Ce_{SN} anomalies start to develop during oxidative weathering and subsequent riverine transport (Byrne and Liu, 1998; Merschel et al., 2017), eventually producing Ce-depleted continental run-off and a negative Ce_{SN} anomaly in seawater (Goldstein and Jacobsen, 1988). Further, a Ce_{SN} anomaly suggested by comparing normalised Ce data to La and Pr can be ambiguous as an environmental proxy, because it may be an artefact of the anomalous enrichment of La in seawater (Bau and Dulski, 1996). Hence, any assessment needs to be based on comparison to Pr_{SN}, Nd_{SN} and/or Sm_{SN} (eg., $(Pr/Pr^*)_{SN}$ >1.05), but must not consider La_{SN} (Fig. 13; Bau and Dulski, 1996; Kamber and Webb, 2001). In that regard the screened samples from B1 show negative Ce_{SN} anomalies with $(Pr/Pr^*)_{SN}$ ratios ranging between 1.06 – 1.36, whereas Units A and C do not record true Ce_{SN} anomalies (Fig. 13). Our interpretation of the true negative Ce_{SN} anomaly in the OnZap carbonate rocks is further strengthened by a persistently negative Ce_{SN} anomaly of similar amplitude in diagenetic apatite from the organic-rich mudstone-dolostone interval in the Shunga outcrop (Fig. 13; Joosu et al., 2015).

555 In the OnZap section, only screened samples from B1 can be considered reliable
556 archives of marine (and, by proxy, atmospheric) composition at the time of deposition, and
557 even then the setting was likely to have been semi-restricted rather than fully open-marine.
558 Hence, based on our REY, Ce and C-isotope data, what can be concluded about the marine
559 water-column in the Onega Basin during deposition of the B1 carbonate rocks is that the
560 oxidative power in the atmosphere-ocean system was strong enough to decouple Ce from other
561 trivalent REE, regardless of whether it occurred during continental weathering or in the marine
562 water-column. Other data, including those of previous workers who have carefully screened
563 their samples (e.g., Črne et al., 2014; Paiste et al., 2018; Kreitsmann et al., 2019), indicate that
564 C- and S-isotope signatures were influenced by basin-specific processes. Thus, our results
565 agree with Mänd et al. (2020) Paiste et al. (2018) and Sheen et al. (2018): namely, that the
566 rocks of the Zaonega Formation recorded varying redox conditions and at least episodically
567 elevated O_2 levels persisting after the LJE. Thus, models and hypotheses about Earth system
568 redox states that use the Zaonega Formation to infer a global collapse of oxygen levels at this
569 time are at best equivocal.

570

571 ## 6. **Conclusions**

572 We presented new high resolution isotopic, trace element, mineralogic, and petrographic
573 characterisation of carbonate beds in a 102-m-thick section recovered in the OnZap drill-cores
574 through the c. 2.0 Ga the upper Zaonega Formation in the Onega Basin, Russia. Our data
575 indicate the following:

576 1) Carbonate beds of the upper Zaonega Formation have mixed carbonate mineralogy.
577 Most of the dolomite in units A and B is better preserved than calcite, although primary
578 calcite is present in Unit A. In Unit C, dolomite is closer to ankerite in composition.

2) Only the middle part of the OnZap section can be used to characterise the isotopic composition of ambient seawater. The screened samples exhibit an upwards increasing shift in $\delta^{13}C_{carb}$ values from -5.4‰ to 0.8‰.
3) Large intra-bed variability suggests a fluctuating influence of methane-derived carbon on the basinal DIC pool.
4) Dolomite in Unit B carries the signal of ambient seawater as suggested by typical seawater REY_{SN} patterns, super-chondritic Y/Ho ratios, LREE depletion compared to HREE and positive La_{SN} and Gd_{SN} anomalies.
5) Negative Ce_{SN} anomalies in samples from B1 require enough oxidative power in the atmosphere-ocean system to oxidise Ce(III) to Ce(IV) and decouple Ce from the other trivalent REE.
6) Consistent positive Eu_{SN} anomalies highlight high-temperature hydrothermal input into local seawater in the Onega Basin during Zaonega times.

In total, these findings contradict previous inferences that the Zaonega Formation witnessed a global collapse of oxygen in the wake of the LJE – instead, we highlight that the atmosphere-ocean system must have retained a significant degree of oxygenation following the LJE.

7. Acknowledgements

We thank P. Fralick, and J. Karhu for insightful comments that improved the manuscript. This study was supported by Estonian Research Council project PRG447, and the Estonian Centre of Analytical Chemistry. K.P. and A.L. were supported by the Research Council of Norway through its Centres of Excellence funding scheme grant No. 223259. K.P. acknowledges the Estonian Research Council grant MOBJD542 and T.M. PUT611. We greatly appreciate the assistance of D. Krämer and F. Klimpel, Jacobs University Bremen, with ICP-MS analyses.

References

Alexander, B.W., Bau, M., Andersson, P., Dulski, P., 2008. Continentally-derived solutes in shallow Archean seawater: Rare earth element and Nd isotope evidence in iron formation from the 2.9Ga Pongola Supergroup, South Africa. Geochim. Cosmochim. Acta 72, 378–394. https://doi.org/10.1016/j.gca.2007.10.028

Alexander, B.W., Bau, M., Andersson, P., 2009. Neodymium isotopes in Archean seawater and implications for the marine Nd cycle in Earth's early oceans. Earth Planet. Sci. Lett. 283, 144–155. https://doi.org/10.1016/j.epsl.2009.04.004

Allwood, A.C., Kamber, B.S., Walter, M.R., Burch, I.W., Kanik, I., 2010. Trace elements record depositional history of an Early Archean stromatolitic carbonate platform. Chem. Geol. 270, 148–163. https://doi.org/10.1016/j.chemgeo.2009.11.013

Asael, D., Tissot, F.L.H., Reinhard, C.T., Rouxel, O., Dauphas, N., Lyons, T.W., Ponzevera, E., Liorzou, C., Chéron, S., 2013. Coupled molybdenum, iron and uranium stable isotopes as oceanic paleoredox proxies during the Paleoproterozoic Shunga Event. Chem. Geol., 362, 193–210. https://doi.org/10.1016/j.chemgeo.2013.08.003

Asael, D., Rouxel, O., Poulton, S.W., Lyons, T.W., Bekker, A., 2018. Molybdenum record from black shales indicates oscillating atmospheric oxygen levels in the early Paleoproterozoic. Am. J. Sci. 318, 275–299. https://doi.org/10.2475/03.2018.01

Bau, M., 1991. Rare-earth element mobility during hydrothermal and metamorphic fluid-rock interaction and the significance of the oxidation state of europium. Chem. Geol. 93, 219–230. https://doi.org/10.1016/0009-2541(91)90115-8

Bau, M., 1993. Effects of syn- and post-depositional processes on the rare-earth element distribution in Precambrian iron-formations. Eur. J. Mineral. 5, 257–267.

Bau, M., Dulski, P., Moeller, P., 1995. Yttrium and holmium in South Pacific seawater: vertical distribution and possible fractionation mechanisms. Chem. Erde - Geochem. 55, 1–15.

629 Bau, M., Dulski, P., 1996. Distribution of yttrium and rare-earth elements in the Penge and
630 Kuruman iron-formations, Transvaal Supergroup, South Africa. Precambrian Res., Geology
631 and Geochemistry of the transvaal supergroup 79, 37–55. https://doi.org/10.1016/0301-
632 9268(95)00087-9
633 Bau, M., Koschinsky, A., Dulski, P., Hein, J.R., 1996. Comparison of the partitioning
634 behaviours of yttrium, rare earth elements, and titanium between hydrogenetic marine
635 ferromanganese crusts and seawater. Geochim. Cosmochim. Acta 60, 1709–1725.
636 https://doi.org/10.1016/0016-7037(96)00063-4
637 Bau, M., Dulski, P., 1999. Comparing Yttrium and rare earths in hydrothermal fluids from the
638 Mid-Atlantic Ridge: implications for Y and REE behaviour during near-vent mixing and for
639 the Y/Ho ratio of Proterozoic seawater. Chem. Geol. 155, 77-90.
640 Bau, M., Alexander, B., 2006. Preservation of primary REE patterns without Ce anomaly
641 during dolomitization of Mid-Paleoproterozoic limestone and the potential re-establishment
642 of marine anoxia immediately after the "Great Oxidation Event." South Afr. J. Geol. 109,
643 81–86. https://doi.org/10.2113/gssajg.109.1-2.81
644 Bau, M., Koschinsky, A., 2009. Oxidative scavenging of cerium on hydrous Fe oxide:
645 Evidence from the distribution of rare earth elements and yttrium between Fe oxides and
646 Mn oxides in hydrogenetic ferromanganese crusts. Geochem. J. 43, 37–47.
647 https://doi.org/10.2343/geochemj.1.0005
648 Bau, M., Balan, S., Schmidt, K., and Koschinsky, A., 2010. Rare earth elements in mussel
649 shells of the *Mytilidae* family as tracers for hidden and fossil high-temperature hydrothermal
650 systems. Earth and Planet. Sci. Lett. 299, 310–316.
651 Bekker, A., Holland, H.D., 2012. Oxygen overshoot and recovery during the early
652 Paleoproterozoic. Earth Planet. Sci. Lett. 317–318, 295–304.
653 https://doi.org/10.1016/j.epsl.2011.12.012

654 Bellefroid, E.J., Hood, A. v S., Hoffman, P.F., Thomas, M.D., Reinhard, C.T., Planavsky, N.J.,
655 2018. Constraints on Paleoproterozoic atmospheric oxygen levels. Proc. Natl. Acad. Sci.
656 115, 8104–8109. https://doi.org/10.1073/pnas.1806216115
657 Bellefroid, E.J., Planavsky, N.J., Hood, A.V.S., Halverson, G.P., Spokas, K., 2019. Shallow
658 water redox conditions of the mid-Proterozoic Muskwa Assemblage, British Columbia,
659 Canada. Am. J. Sci. 319, 122–157. https://doi.org/10.2475/02.2019.03
660 Boetius, A., Ravenschlag, K., Schubert, C.J., Rickert, D., Widdel, F., Gieseke, A., Amann, R.,
661 Jørgensen, B.B., Witte, U., Pfannkuche, O., 2000. A marine microbial consortium
662 apparently mediating anaerobic oxidation of methane. Nature 407, 623–626.
663 https://doi.org/10.1038/35036572
664 Bolhar, R., Kamber, B.S., Moorbath, S., Fedo, C.M., Whitehouse, M.J., 2004. Characterisation
665 of early Archaean chemical sediments by trace element signatures. Earth Planet. Sci. Lett.
666 222, 43–60. https://doi.org/10.1016/j.epsl.2004.02.016
667 Bolhar, R., Van Kranendonk, M.J., 2007. A non-marine depositional setting for the northern
668 Fortescue Group, Pilbara Craton, inferred from trace element geochemistry of stromatolitic
669 carbonates. Precambrian Res. 155, 229–250.
670 https://doi.org/10.1016/j.precamres.2007.02.002
671 Brand, U., Veizer, J., 1980. Chemical diagenesis of a multicomponent carbonate system - 1.
672 Trace elements. J. Sediment. Petrol. 50, 1219–1236. https://doi.org/10.1306/212F7BB7-
673 2B24-11D7-8648000102C1865D
674 Brasier, A.T., Fallick, A.E., Prave, A.R., Melezhik, V.A., Lepland, A., 2011. Coastal sabkha
675 dolomites and calcitised sulfates preserving the Lomagundi-Jatuli carbon isotope signal.
676 Precambrian Res. 189, 193–211. https://doi.org/10.1016/j.precamres.2011.05.011

677 Byrne, R.H., Liu, X., 1998. A Coupled Riverine-Marine Fractionation Model for Dissolved
678 Rare Earths and Yttrium. Aquat. Geochem. 4, 103–121.
679 https://doi.org/10.1023/A:1009651919911
680 Campbell, K.A., 2006. Hydrocarbon seep and hydrothermal vent paleoenvironments and
681 paleontology: Past developments and future research directions. Palaeogeogr.
682 Palaeoclimatol. Palaeoecol. 232, 362–407. https://doi.org/10.1016/j.palaeo.2005.06.018
683 Canfield, D.E., Ngombi-Pemba, L., Hammarlund, E.U., Bengtson, S., Chaussidon, M.,
684 Gauthier-Lafaye, F., Meunier, A., Riboulleau, A., Rollion-Bard, C., Rouxel, O., Asael, D.,
685 Pierson-Wickmann, A.-C., Albani, A.E., 2013. Oxygen dynamics in the aftermath of the
686 Great Oxidation of Earth's atmosphere. Proc. Natl. Acad. Sci. 110, 16736–16741.
687 https://doi.org/10.1073/pnas.1315570110
688 Castellini, D.G., Dickens, G.R., Snyder, G.T., Ruppel, C.D., 2006. Barium cycling in shallow
689 sediment above active mud volcanoes in the Gulf of Mexico. Chem. Geol. 226, 1–30.
690 https://doi.org/10.1016/j.chemgeo.2005.08.008
691 Črne, A.E., Melezhik, V.A., Prave, A.R., Lepland, A., Romashkin, A.E., Rychanchik, D.V.,
692 Hanski, E.J., Luo, Z., 2013. Zaonega formation: FAR-DEEP hole 13A. In: Melezhik, V.A.,
693 Prave, A.R., Fallick, A.E., Hanski, E.J., Lepland, A., Kump, L.R., Strauss, H. (Eds),
694 Reading the Archive of Earth`s Oxygenation: Volume 2: The Core Archive of the
695 Fennoscandian Arctic Russia – Drilling Early Earth Project. Springer, pp. 1008-1046.
696 https://doi.org/10.1007/978-3-642-29659-8_4
697 Črne, A.E., Melezhik, V.A., Lepland, A., Fallick, A.E., Prave, A.R., Brasier, A.T., 2014.
698 Petrography and geochemistry of carbonate rocks of the Paleoproterozoic Zaonega
699 Formation, Russia: Documentation of ^{13}C-depleted non-primary calcite. Precambrian Res.
700 240, 79–93. https://doi.org/10.1016/j.precamres.2013.10.005

Derry, L.A., 2010. A burial diagenesis origin for the Ediacaran Shuram-Wonoka carbon isotope anomaly. Earth Planet. Sci. Lett., 294, 152–162. https://doi.org/10.1016/j.epsl.2010.03.022

Douville, E., Bienvenu, P., Charlou, J.L., Donval, J.P., Fouquet, Y., Appriou, P., Gamo, T., 1999. Yttrium and rare earth elements in fluids from various deep-sea hydrothermal systems. Geochim. Cosmochim. Acta 63, 627–643. https://doi.org/10.1016/S0016-7037(99)00024-1

Elderfield, H., Greaves, J. M., 1982. The rare earth elements in seawater. Nature 296, 214-219. https://doi.org/10.1038/296214a0

Elderfield, H., Whitfield, M., Burton, J.D., Bacon, M.P., Liss, P.S., Charnock, H., Lovelock, J.E., Whitfield, M., 1988. The oceanic chemistry of the rare-earth elements. Philos. Trans. R. Soc. Lond. Ser. Math. Phys. Sci. 325, 105–126. https://doi.org/10.1098/rsta.1988.0046

Frimmel, H.E., 2009. Trace element distribution in Neoproterozoic carbonates as palaeoenvironmental indicator. Chem. Geol. 258, 338–353. https://doi.org/10.1016/j.chemgeo.2008.10.033

Geilert, S., Hensen, C., Schmidt, M., Liebetrau, V., Scholz, F., Doll, M., Deng, L., Fiskal, A., Lever, M.A., Su, C.-C., Schloemer, S., Sarkar, S., Thiel, V., Berndt, C., 2018. On the formation of hydrothermal vents and cold seeps in the Guaymas Basin, Gulf of California. Biogeosciences 15, 5715–5731. https://doi.org/10.5194/bg-15-5715-2018

Goldstein, S.J., Jacobsen, S.B., 1988. Rare earth elements in river waters. Earth Planet. Sci. Lett. 89, 35–47. https://doi.org/10.1016/0012-821X(88)90031-3

Griffith, E.M., Paytan, A., 2012. Barite in the ocean – occurrence, geochemistry and palaeoceanographic applications. Sedimentology 59, 1817–1835. https://doi.org/10.1111/j.1365-3091.2012.01327.x

724 Himmler, T., Bach, W., Bohrmann, G., Peckmann, J., 2010. Rare earth elements in authigenic
725 methane-seep carbonates as tracers for fluid composition during early diagenesis. Chem.
726 Geol. 277, 126–136. https://doi.org/10.1016/j.chemgeo.2010.07.015
727 Holland, H.D., 2006. The oxygenation of the atmosphere and oceans. Philos. Trans. R. Soc. B
728 Biol. Sci. 361, 903–915. https://doi.org/10.1098/rstb.2006.1838
729 Irwin, H., Curtis, C., Coleman, M., 1977. Isotopic evidence for source of diagenetic carbonates
730 formed during burial of organic-rich sediments. Nature 269, 209.
731 https://doi.org/10.1038/269209a0
732 Jacobsen, S.B., Kaufman, A.J., 1999. The Sr, C and O isotopic evolution of Neoproterozoic
733 seawater. Chem. Geol. 161, 37–57. https://doi.org/10.1016/S0009-2541(99)00080-7
734 Joosu, L., Lepland, A., Kirsimäe, K., Romashkin, A.E., Roberts, N.M.W., Martin, A.P., Črne,
735 A.E., 2015. The REE-composition and petrography of apatite in 2Ga Zaonega Formation,
736 Russia: The environmental setting for phosphogenesis. Chem. Geol. 395, 88–107.
737 https://doi.org/10.1016/j.chemgeo.2014.11.013
738 Joye, S.B., Bowles, M.W., Samarkin, V.A., Hunter, K.S., Niemann, H., 2010. Biogeochemical
739 signatures and microbial activity of different cold-seep habitats along the Gulf of Mexico
740 deep slope. Deep Sea Res. Part II Top. Stud. Oceanogr., Gulf of Mexico Cold Seeps 57,
741 1990–2001. https://doi.org/10.1016/j.dsr2.2010.06.001
742 Kamber, B.S., Webb, G.E., 2001. The geochemistry of late Archaean microbial carbonate:
743 implications for ocean chemistry and continental erosion history. Geochim. Cosmochim.
744 Acta 65, 2509–2525. https://doi.org/10.1016/S0016-7037(01)00613-5
745 Kamber, B.S., Webb, G.E., Gallagher, M., 2014. The rare earth element signal in Archaean
746 microbial carbonate: information on ocean redox and biogenicity. J. Geol. Soc. 171, 745–
747 763. https://doi.org/10.1144/jgs2013-110

748 Karhu, J.A., 1993. Paleoproterozoic evolution of the carbon isotope ratios of sedimentary
749 carbonates in the Fennoscandian Shield. Geologian tutkimuskeskus.
750 Karhu, J.A., Holland, H.D., 1996. Carbon isotopes and the rise of atmospheric oxygen.
751 Geology 24, 867–870. https://doi.org/10.1130/0091-
752 7613(1996)024<0867:CIATRO>2.3.CO;2
753 Kasting, J.F., 2001. The Rise of Atmospheric Oxygen. Science 293, 819–820.
754 https://doi.org/10.1126/science.1063811
755 Kaufman, A.J., Knoll, A.H., 1995. Neoproterozoic variations in the C-isotopic composition of
756 seawater: stratigraphic and biogeochemical implications. Precambrian Res., 73, 27–49.
757 https://doi.org/10.1016/0301-9268(94)00070-8
758 Kipp, M.A., Stüeken, E.E., Bekker, A., Buick, R., 2017. Selenium isotopes record extensive
759 marine suboxia during the Great Oxidation Event. Proc. Natl. Acad. Sci. 114, 875–880.
760 https://doi.org/10.1073/pnas.1615867114
761 Koistinen, T., Stephens, M.B., Bogatchev, V., Nordgulen, Ø., Wenneström, M., Korhonen, J.,
762 2001. Geological Map of the Fennoscandian Shield. In: Scale 1:2,000,000. Norway and
763 Sweden and the North-West Department of Natural Resources of Russia, Geological
764 Surveys of Finland
765 Kreitsmann, T., Külaviir, M., Lepland, A., Paiste, K., Paiste, P., Prave, A.R., Sepp, H.,
766 Romashkin, A.E., Rychanchik, D.V., Kirsimäe, K., 2019. Hydrothermal dedolomitisation
767 of carbonate rocks of the Paleoproterozoic Zaonega Formation, NW Russia — Implications
768 for the preservation of primary C isotope signals. Chem. Geol. 512, 43–57.
769 https://doi.org/10.1016/j.chemgeo.2019.03.002
770 Kump, L.R., Junium, C., Arthur, M.A., Brasier, A., Fallick, A., Melezhik, V., Lepland, A.,
771 Črne, A.E., Luo, G., 2011. Isotopic Evidence for Massive Oxidation of Organic Matter

772 Following the Great Oxidation Event. Science 334, 1694–1696.
773 https://doi.org/10.1126/science.1213999
774 Lepland, A., Joosu, L., Kirsimäe, K., Prave, A.R., Romashkin, A.E., Črne, A.E., Martin, A.P.,
775 Fallick, A.E., Somelar, P., Üpraus, K., Mänd, K., Roberts, N.M.W., Van, Z., Wirth, R.,
776 Schreiber, A., 2014. Potential influence of sulphur bacteria on Palaeoproterozoic
777 phosphogenesis. Nat. Geosci. 7, 20–24. https://doi.org/10.1038/ngeo2005
778 Liu, X.-M., Hardisty, D.S., Lyons, T.W., Swart, P.K., 2019. Evaluating the fidelity of the
779 cerium paleoredox tracer during variable carbonate diagenesis on the Great Bahamas Bank.
780 Geochim. Cosmochim. Acta 248, 25–42. https://doi.org/10.1016/j.gca.2018.12.028
781 Lyons, T.W., Reinhard, C.T., Planavsky, N.J., 2014. The rise of oxygen in Earth's early ocean
782 and atmosphere. Nature 506, 307. https://doi.org/10.1038/nature13068
783 Martin, A.P., Condon, D.J., Prave, A.R., Lepland, A., 2013. A review of temporal constraints
784 for the Palaeoproterozoic large, positive carbonate carbon isotope excursion (the
785 Lomagundi–Jatuli Event). Earth-Sci. Rev. 127, 242–261.
786 https://doi.org/10.1016/j.earscirev.2013.10.006
787 Martin, A.P., Prave, A.R., Condon, D.J., Lepland, A., Fallick, A.E., Romashkin, A.E.,
788 Medvedev, P.V., Rychanchik, D.V., 2015. Multiple Palaeoproterozoic carbon burial
789 episodes and excursions. Earth Planet. Sci. Lett. 424, 226–236.
790 https://doi.org/10.1016/j.epsl.2015.05.023
791 Mazzullo, S.J., 2000. Organogenic Dolomitization in Peritidal to Deep-Sea Sediments. J.
792 Sediment. Res. 70, 10–23. https://doi.org/10.1306/2DC408F9-0E47-11D7-
793 8643000102C1865D
794 McLennan, S.M., 1989. Rare earth elements in sedimentary rocks; influence of provenance and
795 sedimentary processes. Rev. Mineral. Geochem. 21, 169–200.

796 Melezhik, V.A., Fallick, A.E., Filippov, M.M., Larsen, O., 1999. Karelian shungite—an
797 indication of 2.0-Ga-old metamorphosed oil-shale and generation of petroleum: geology,
798 lithology and geochemistry. Earth-Sci. Rev. 47, 1–40. https://doi.org/10.1016/S0012-
799 8252(99)00027-6
800 Melezhik, V.A., Huhma, H., Condon, D.J., Fallick, A.E., Whitehouse, M.J., 2007. Temporal
801 constraints on the Paleoproterozoic Lomagundi-Jatuli carbon isotopic event. Geology 35,
802 655–658. https://doi.org/10.1130/G23764A.1
803 Melezhik, V.A., Fallick, A.E., Brasier, A.T., Lepland, A., 2015. Carbonate deposition in the
804 Palaeoproterozoic Onega basin from Fennoscandia: a spotlight on the transition from the
805 Lomagundi-Jatuli to Shunga events. Earth-Sci. Rev. 147, 65–98.
806 https://doi.org/10.1016/j.earscirev.2015.05.005
807 Merschel, G.and Bau, M., 2015. Rare earth elements in the aragonitic shell of freshwater
808 mussel *Corbicula fluminea* and the bioavailability of anthropogenic lanthanum, samarium
809 and gadolinium in river water. Science of the Total Environment 533, 91–101.
810 Merschel, G., Bau, M., Schmidt, K., Münker, C., Dantas, E.L., 2017. Hafnium and neodymium
811 isotopes and REY distribution in the truly dissolved, nanoparticulate/colloidal and
812 suspended loads of rivers in the Amazon Basin, Brazil. Geochim. Cosmochim. Acta 213,
813 383–399. https://doi.org/10.1016/j.gca.2017.07.006
814 Mänd, K., Robbins, L. J., Thoby, M., Paiste, K., Kreitsmann, T., Lalonde, S.V., Kirsimäe, K.,
815 Lepland, A., Konhauser, K.O., 2020. Extreme trace metal enrichments in the Zaonega
816 Formation indicate a post-Lomagundi O_2 overshoot. Nat. Geosci. 13, 302–306.
817 https://doi.org/10.1038/s41561-020-0558-5
818 Nozaki, Y., Zhang, J., Amakawa, H., 1997. The fractionation between Y and Ho in the marine
819 environment. Earth Planet. Sci. Lett. 148, 329–340. https://doi.org/10.1016/S0012-
820 821X(97)00034-4

821 Orphan, V.J., House, C.H., Hinrichs, K.-U., McKeegan, K.D., DeLong, E.F., 2002. Multiple
822 archaeal groups mediate methane oxidation in anoxic cold seep sediments. Proc. Natl. Acad.
823 Sci. U. S. A. 99, 7663–7668. https://doi.org/10.1073/pnas.072210299
824 Ossa Ossa, F., Eickmann, B., Hofmann, A., Planavsky, N.J., Asael, D., Pambo, F., Bekker, A.,
825 2018. Two-step deoxygenation at the end of the Paleoproterozoic Lomagundi Event. Earth
826 Planet. Sci. Lett. 486, 70–83. https://doi.org/10.1016/j.epsl.2018.01.009
827 Paiste, K., Lepland, A., Zerkle, A.L., Kirsimäe, K., Izon, G., Patel, N.K., McLean, F.,
828 Kreitsmann, T., Mänd, K., Bui, T.H., Romashkin, A.E., Rychanchik, D.V., Prave, A.R.,
829 2018. Multiple sulphur isotope records tracking basinal and global processes in the 1.98 Ga
830 Zaonega Formation, NW Russia. Chem. Geol. 499, 151–164.
831 https://doi.org/10.1016/j.chemgeo.2018.09.025
832 Paiste, K., Pellerin, A., Zerkle, A.L., Kirsimäe, K., Prave, A.R., Romashkin, A.E., Lepland, A.,
833 2020. The pyrite multiple sulfur isotope record of the 1.98 Ga Zaonega Formation: Evidence
834 for biogeochemical sulfur cycling in a semi-restricted basin. Earth and Planet. Sci. Lett. 534,
835 116092. https://doi.org/10.1016/j.epsl.2020.116092
836 Partin, C.A., Bekker, A., Planavsky, N.J., Scott, C.T., Gill, B.C., Li, C., Podkovyrov, V.,
837 Maslov, A., Konhauser, K.O., Lalonde, S.V., Love, G.D., Poulton, S.W., Lyons, T.W.,
838 2013. Large-scale fluctuations in Precambrian atmospheric and oceanic oxygen levels from
839 the record of U in shales. Earth Planet. Sci. Lett. 369–370, 284–293.
840 https://doi.org/10.1016/j.epsl.2013.03.031
841 Planavsky, N.J., Bekker, A., Hofmann, A., Owens, J.D., Lyons, T.W., 2012. Sulfur record of
842 rising and falling marine oxygen and sulfate levels during the Lomagundi event. Proc. Natl.
843 Acad. Sci. 109, 18300–18305. https://doi.org/10.1073/pnas.1120387109
844 Préat, A., Bouton, P., Thiéblemont, D., Prian, J.-P., Ndounze, S.S., Delpomdor, F., 2011.
845 Paleoproterozoic high $\delta^{13}C$ dolomites from the Lastoursville and Franceville basins (SE

Gabon): Stratigraphic and synsedimentary subsidence implications. Precambrian Res. 189, 212–228. https://doi.org/10.1016/j.precamres.2011.05.013

Puchtel, I.S., Brügmann, G.E., Hofmann, A.W., 1999. Precise Re–Os mineral isochron and Pb–Nd–Os isotope systematics of a mafic–ultramafic sill in the 2.0 Ga Onega plateau (Baltic Shield). Earth Planet. Sci. Lett. 170, 447–461. https://doi.org/10.1016/S0012-821X(99)00118-1

Qu, Y., Črne, A.E., Lepland, A., van Zuilen, M.A., 2012. Methanotrophy in a Paleoproterozoic oil field ecosystem, Zaonega Formation, Karelia, Russia. Geobiology 10, 467–478. https://doi.org/10.1111/gbi.12007

Qu, Y., Lepland, A., van Zuilen, M.A., Whitehouse, M., Črne, A.E., Fallick, A.E., 2018. Sample-scale carbon isotopic variability and diverse biomass in the Paleoproterozoic Zaonega Formation, Russia. Precambrian Res. 315, 222–231. https://doi.org/10.1016/j.precamres.2018.07.008

Raiswell, R., Fisher, Q.J., 2000. Mudrock-hosted carbonate concretions: a review of growth mechanisms and their influence on chemical and isotopic composition. J. Geol. Soc., London 157, 239-251. https://doi.org/10.1144/jgs.157.1.239

Rosenbaum, J., Sheppard, S.M.F., 1986. An isotopic study of siderites, dolomites and ankerites at high temperatures. Geochim. Cosmochim. Acta 50, 1147–1150. https://doi.org/10.1016/0016-7037(86)90396-0

Sapart, C.J., Monteil, G., Prokopiou, M., van de Wal, R.S.W., Kaplan, J.O., Sperlich, P., Krumhardt, K.M., van der Veen, C., Houweling, S., Krol, M.C., Blunier, T., Sowers, T., Martinerie, P., Witrant, E., Dahl-Jensen, D., Röckmann, T., 2012. Natural and anthropogenic variations in methane sources during the past two millennia. Nature 490, 85–88. https://doi.org/10.1038/nature11461

870 Schidlowski, M., Eichmann, R., Junge, C.E., 1976. Carbon isotope geochemistry of the
871 Precambrian Lomagundi carbonate province, Rhodesia. Geochim. Cosmochim. Acta 40,
872 449–455. https://doi.org/10.1016/0016-7037(76)90010-7
873 Schidlowski, M., 2001. Carbon isotopes as biogeochemical recorders of life over 3.8 Ga of
874 Earth history: evolution of a concept. Precambrian Res. 106, 117–134.
875 https://doi.org/10.1016/S0301-9268(00)00128-5
876 Schier, K., Bau, M., Münker, C., Beukes, N., Viehmann, S., 2018. Trace element and Nd
877 isotope composition of shallow seawater prior to the Great Oxidation Event: Evidence from
878 stromatolitic bioherms in the Paleoproterozoic Rooinekke and Nelani Formations, South
879 Africa. Precambrian Res. 315, 92–102. https://doi.org/10.1016/j.precamres.2018.07.014
880 Schoell, M., 1988. Multiple origins of methane in the Earth. Chem. Geol., Origins of Methane
881 in the Earth 71, 1–10. https://doi.org/10.1016/0009-2541(88)90101-5
882 Scott, C., Wing, B.A., Bekker, A., Planavsky, N.J., Medvedev, P., Bates, S.M., Yun, M., Lyons,
883 T.W., 2014. Pyrite multiple-sulfur isotope evidence for rapid expansion and contraction of
884 the early Paleoproterozoic seawater sulfate reservoir. Earth Planet. Sci. Lett. 389, 95–104.
885 https://doi.org/10.1016/j.epsl.2013.12.010
886 Sheen, A.I., Kendall, B., Reinhard, C.T., Creaser, R.A., Lyons, T.W., Bekker, A., Poulton,
887 S.W., Anbar, A.D., 2018. A model for the oceanic mass balance of rhenium and implications
888 for the extent of Proterozoic ocean anoxia. Geochim. Cosmochim. Acta 227, 75–95.
889 https://doi.org/10.1016/j.gca.2018.01.036
890 Shields, G., Stille, P., 2001. Diagenetic constraints on the use of cerium anomalies as
891 palaeoseawater redox proxies: an isotopic and REE study of Cambrian phosphorites. Chem.
892 Geol., Response of the Oceanic / Atmospheric Systems to Past Global Changes 175, 29–48.
893 https://doi.org/10.1016/S0009-2541(00)00362-4

894 Simoneit, B.R.T., Lonsdale, P.F., Edmond, J.M., Shanks, W.C., 1990. Deep-water hydrocarbon
895 seeps in Guaymas Basin, Gulf of California. Appl. Geochem., Organic Matter in
896 Hyrothermal Systems—Maturation, Migration and Biogeochemistry 5, 41–49.
897 https://doi.org/10.1016/0883-2927(90)90034-3
898 Strauss, H., Melezhik, V.A., Lepland, A., Fallick, A.E., Hanski, E.J., Filippov, M.M., Deines,
899 Y.E., Illing, C.J., Črne, A.E., Brasier, A.T., 2013. 7.6 Enhanced Accumulation of Organic
900 Matter: The Shunga Event, in: Melezhik, V.A., Prave, A.R., Hanski, E.J., Fallick, A.E.,
901 Lepland, A., Kump, L.R., Strauss, H. (Eds.), Reading the Archive of Earth's Oxygenation:
902 Volume 3: Global Events and the Fennoscandian Arctic Russia - Drilling Early Earth
903 Project, Frontiers in Earth Sciences. Springer,1195–1273. https://doi.org/10.1007/978-3-
904 642-29670-3_6
905 Svensen, H., Planke, S., Jamtveit, B., Pedersen, T., 2003. Seep carbonate formation controlled
906 by hydrothermal vent complexes: a case study from the Vøring Basin, the Norwegian Sea.
907 Geo-Mar. Lett. 23, 351–358. https://doi.org/10.1007/s00367-003-0141-2
908 Sverjensky, A.D., 1984. Europium redox equilibria in aqueous solution. Earth Planet. Sci. Lett.,
909 67, 70-78. https://doi.org/10.1016/0012-821X(84)90039-6
910 Swart, P.K., 2015. The geochemistry of carbonate diagenesis: The past, present and future.
911 Sedimentology 62, 1233–1304. https://doi.org/10.1111/sed.12205
912 Taylor, S.R., McLennan, S.M., 1985. The Continental Crust, Its Composition and Evolution.
913 Blackwell Scientific Publications, Oxford, UK.
914 Tostevin, R., Shields, G.A., Tarbuck, G.M., He, T., Clarkson, M.O., Wood, R.A., 2016.
915 Effective use of cerium anomalies as a redox proxy in carbonate-dominated marine settings.
916 Chem. Geol. 438, 146–162. https://doi.org/10.1016/j.chemgeo.2016.06.027
917 Veizer, J., 1983. Trace elements and isotopes in sedimentary carbonates. Rev. Mineral.
918 Geochem. 11, 265–299.

919 Viehmann, S., Bau, M., Hoffmann, J.E., Münker, C., 2015a. Geochemistry of the Krivoy Rog
920 Banded Iron Formation, Ukraine, and the impact of peak episodes of increased global
921 magmatic activity on the trace element composition of Precambrian seawater. Precambrian
922 Res. 270, 165–180. https://doi.org/10.1016/j.precamres.2015.09.015
923 Viehmann, S., Bau, M., Smith, A.J.B., Beukes, N.J., Dantas, E.L., Bühn, B., 2015b. The
924 reliability of ~2.9 Ga old Witwatersrand banded iron formations (South Africa) as archives
925 for Mesoarchean seawater: Evidence from REE and Nd isotope systematics. J. Afr. Earth
926 Sci. 111, 322–334. https://doi.org/10.1016/j.jafrearsci.2015.08.013
927 Wang, W., Bolhar, R., Zhou, M.-F., Zhao, X.-F., 2018. Enhanced terrestrial input into
928 Paleoproterozoic to Mesoproterozoic carbonates in the southwestern South China Block
929 during the fragmentation of the Columbia supercontinent. Precambrian Res. 313, 1–17.
930 https://doi.org/10.1016/j.precamres.2018.05.001
931 Webb, G.E., Kamber, B.S., 2000. Rare earth elements in Holocene reefal microbialites: a new
932 shallow seawater proxy. Geochim. Cosmochim. Acta 64, 1557–1565.
933 https://doi.org/10.1016/S0016-7037(99)00400-7
934 Whiticar, M.J., 1999. Carbon and hydrogen isotope systematics of bacterial formation and
935 oxidation of methane. Chem. Geol. 161, 291–314. https://doi.org/10.1016/S0009-
936 2541(99)00092-3
937 Wright, J., Schrader, H., Holser, T.W., 1987. Paleoredox variations in ancient oxeans recorded
938 by rare earth elements in fossil apatite. Geochim. Cosmochim. Acta 51, 631-644.
939 https://doi.org/10.1016/0016-7037(87)90075-5
940 Zhao, M.-Y., Zheng, Y.-F., 2017. A geochemical framework for retrieving the linked
941 depositional and diagenetic histories of marine carbonates. Earth Planet. Sci. Lett. 460, 213–
942 221. https://doi.org/10.1016/j.epsl.2016.11.033
943

944 # Tables

Table 1. Carbonate bed intervals in OnZap composite section with average carbonate mineralogy and isotopic values. B.d. Stands for below detection (<0.5 wt.%)

Carbonate bed interval	Depth (m)	Lithology	Calcite (wt.%)	Dolomite (wt.%)	$\delta^{13}C_{carb}$ (‰, VPDB)	$\delta^{18}O$ (‰, VPDB)
A1	101.39 - 100.75	Calcareous mudstone	48.0 ± 12.5	7.8 ± 6.9	-18.23 ± 4.6	-13.1 ± 0.8
A2	97.28 - 96.74	Calcareous mudstone	37.8 ± 9.1	b.d.	-22.2 ± 2.9	-14.0 ± 0.2
A3	93.1 - 93.82	Calcareous mudstone	36.7 ± 14.0	b.d.	-10.2 ± 1.0	-13.8 ± 0.3
A4	86.12 - 77.53	Calcareous mudstone	21.7 ± 17.8	25.0 ± 17.7	-14.3 ± 3.0	-13.5 ± 0.4
A5	75.43 - 55.47	Dolostone	33.2 ± 22.7	36.1 ± 32.6	-13.8 ± 3.4	-13.1 ± 0.8
B1	52.47 - 41.49	Dolostone	8.3 ± 17.5	78.9 ± 22.7	-6.6 ± 3.4	-11.7 ± 1.5
B2	40.12 - 38.8	Calcareous mudstone	32.6 ± 10.9	b.d.	-13.8 ± 1.3	-13.3 ± 0.2
B3	37.65 - 33.06	Dolostone	9.6 ± 15.0	77.0 ± 21.6	-6.3 ± 2.9	-10.8 ± 1.3
C1	32.91 - 30.06	Dolostone	2.0 ± 2.5	80.3 ± 20.4	-3.0 ± 2.6	-9.6 ± 1.8
C2	29.8 - 15.9	Dolostone	3.2 ± 3.3	71.4 ± 12.2	-4.7 ± 0.6	-11.7 ± 0.6
C3	15.25 - 7.86	Calcareous mudstone	1.05 ± 1.4	57.7 ± 17.3	-6.2 ± 0.9	-12.6 ± 0.4

945

946

947

948

949

950

951

952

953

954

955

956

957

Figures

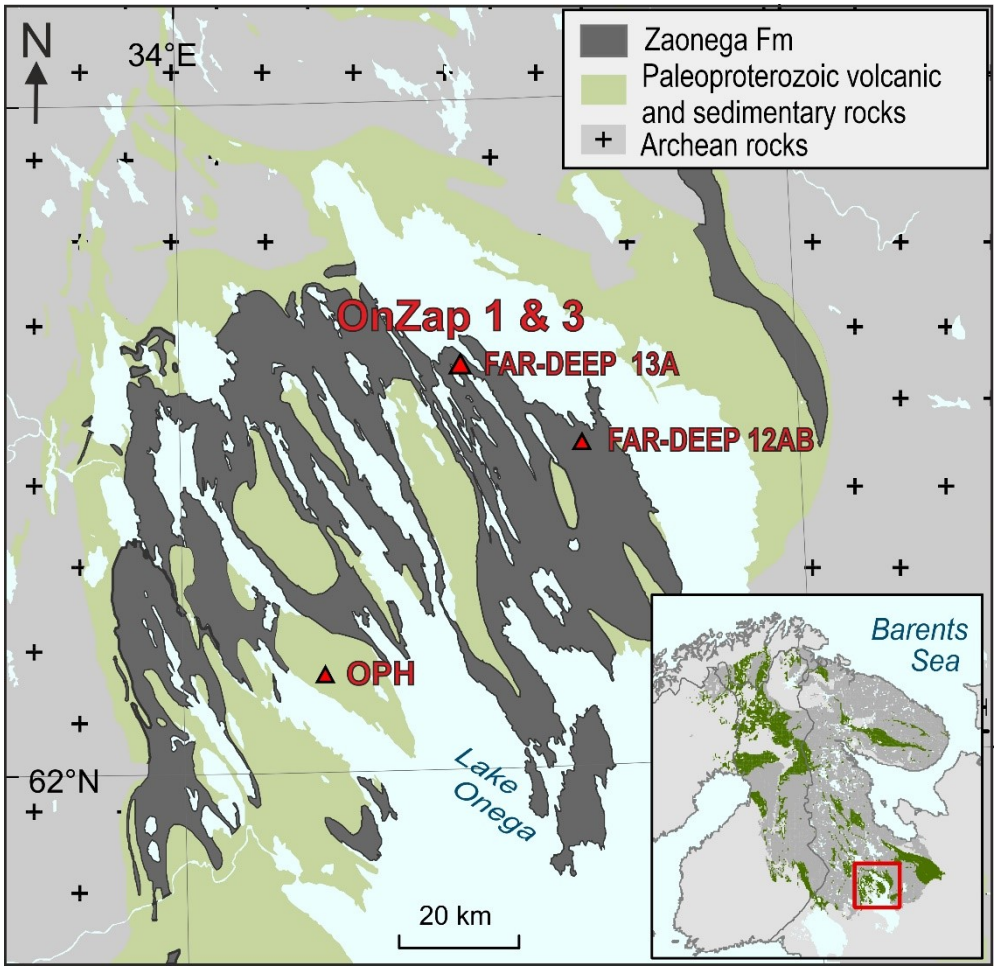

Figure 1. Simplified geological map of the Onega Basin in NW Russia (after Koistinen et al., 2001). Drill-core locations are shown as red triangles. FAR-DEEP 13A and OnZap drill-cores were drilled 500 m apart. OPH – Onega Parametric Hole.

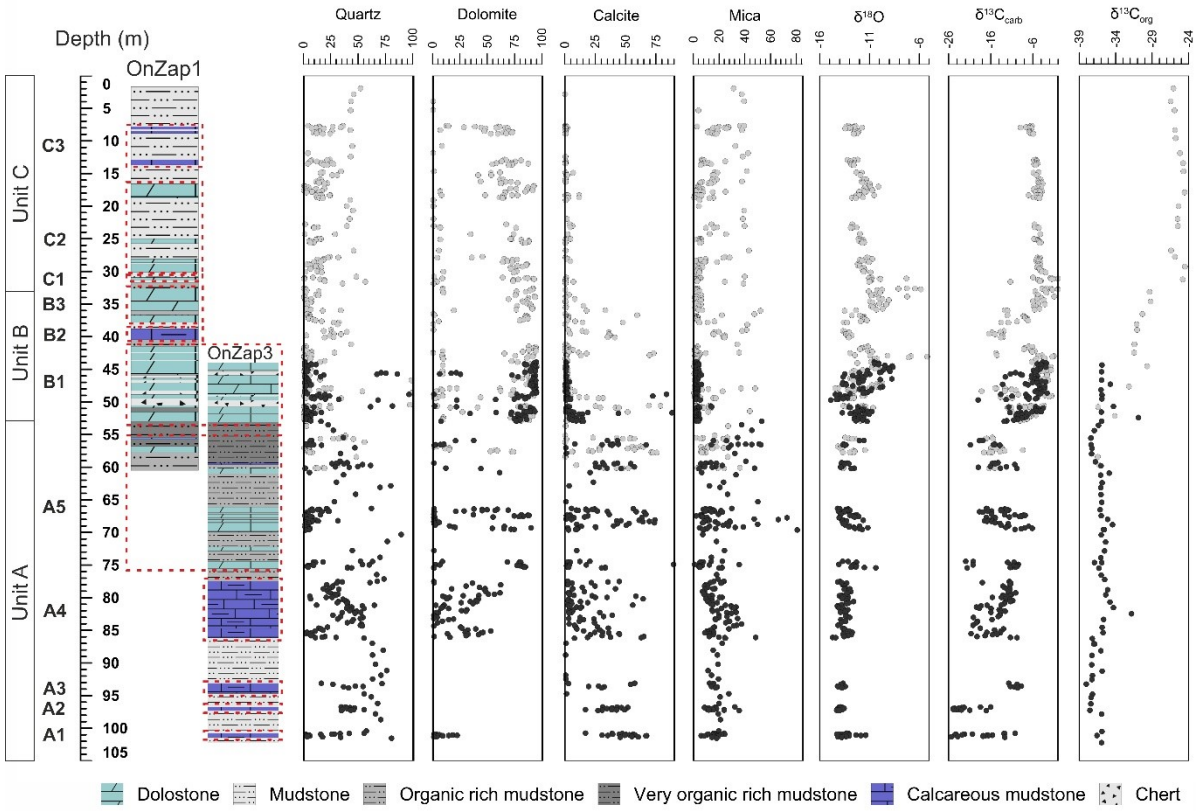

964

965 **Figure 2.** Lithostratigraphic column of the OnZap section with quartz, dolomite, calcite and

966 mica abundances in wt.% and isotopic values of carbonate $\delta^{18}O$ and $\delta^{13}C$ (‰, VPDB). $\delta^{13}C_{org}$

967 (‰, VPDB) data are from Paiste et al. (2018). Dashed red boxes outline carbonate intervals

968 A1 to C3.

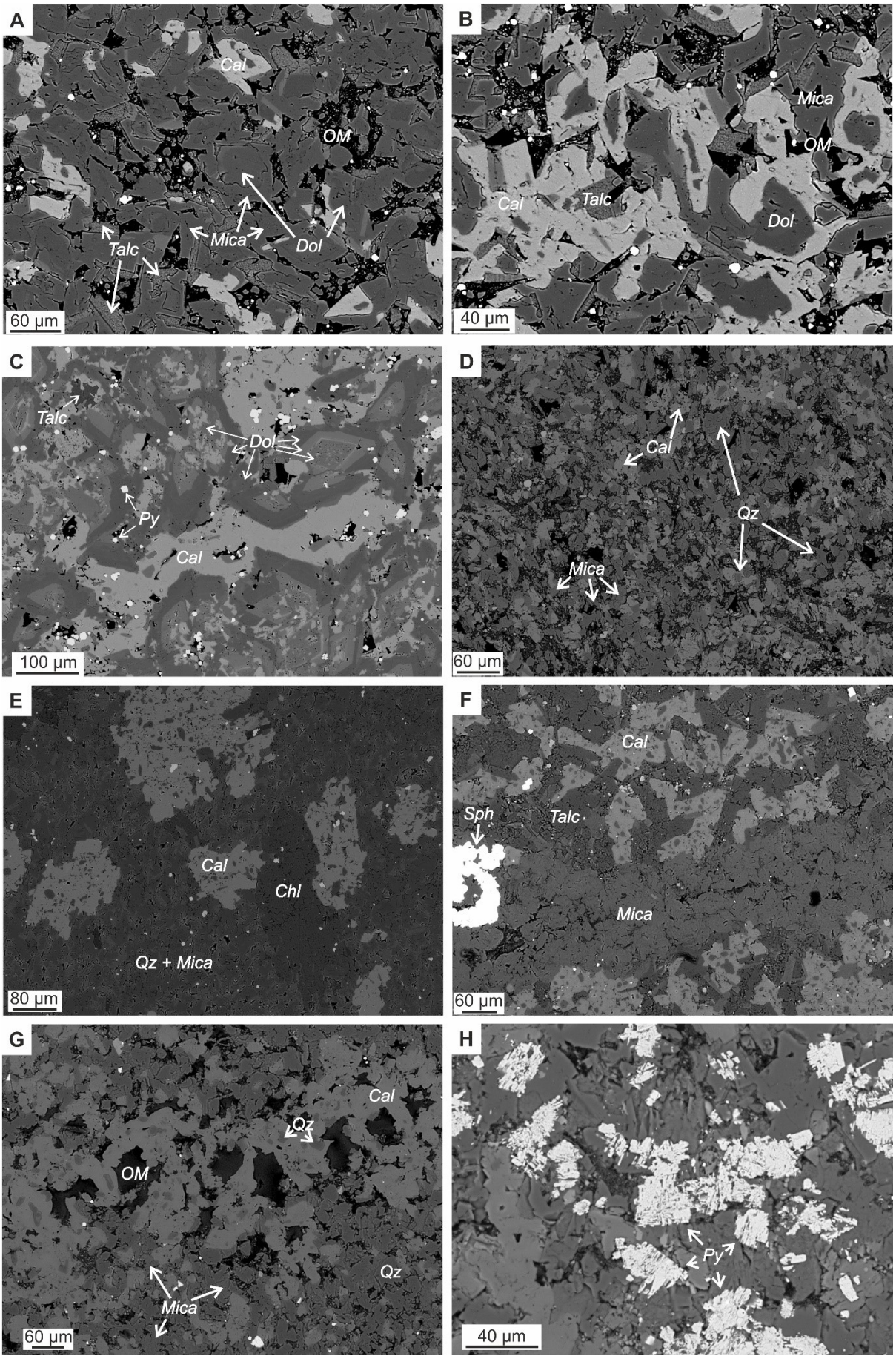
A
Cal
OM
Talc
Mica
Dol
60 µm
B
Mica
OM
Cal
Talc
Dol
40 µm
C
Talc
Dol
Py
Cal
100 µm
D
Cal
Qz
Mica
60 µm
E
Cal
Chl
Qz + Mica
80 µm
F
Cal
Sph
Talc
Mica
60 µm
G
Cal
Qz
OM
Qz
Mica
60 µm
H
Py
40 µm

969

Figure 3. SEM images in back-scatter detector (BSD) mode characterising carbonate rocks in Unit A. (A) Small (<100 μm) planar-s dolomite crystals with abundant talc and mica. Calcite is replacing dolomite; A5, depth 74.54 m. (B) Pseudomorphic calcite replacing dolomite via dedolomitisation; A5, depth 74.54 m. (C) Zoned dolomite crystals with cloudier cores and later pore-filling and intracrystalline calcite formed via dedolomitisation; A5, depth 57.38 m. (D) Calcite cement representing primary carbonate of methane derived origin. Note the abundance of mica, quartz grains and the absence of talc and dolomite; A2, depth 97.19 m. (E) Probable metamorphic calcite and large chlorite crystals that cross-cut the bedding. Calcite has a poikilitic texture with quartz and pyrite inclusions; A4, depth 84.4 m. (F) Larger elongated methane derived calcite crystals with quartz and dolomite inclusions; A1, depth 101.22 m. (G) Possible conduits for fluid and hydrocarbon flow that are filled with massive organic matter and surrounded by calcite; A2 depth 96.95 m. (H) Skeletal pyrite pseudomorphs after barite; A2 depth 96.95 m. Cal – calcite, Dol – dolomite, Py – pyrite, OM – organic matter, Qz – quartz, Sph – sphalerite.

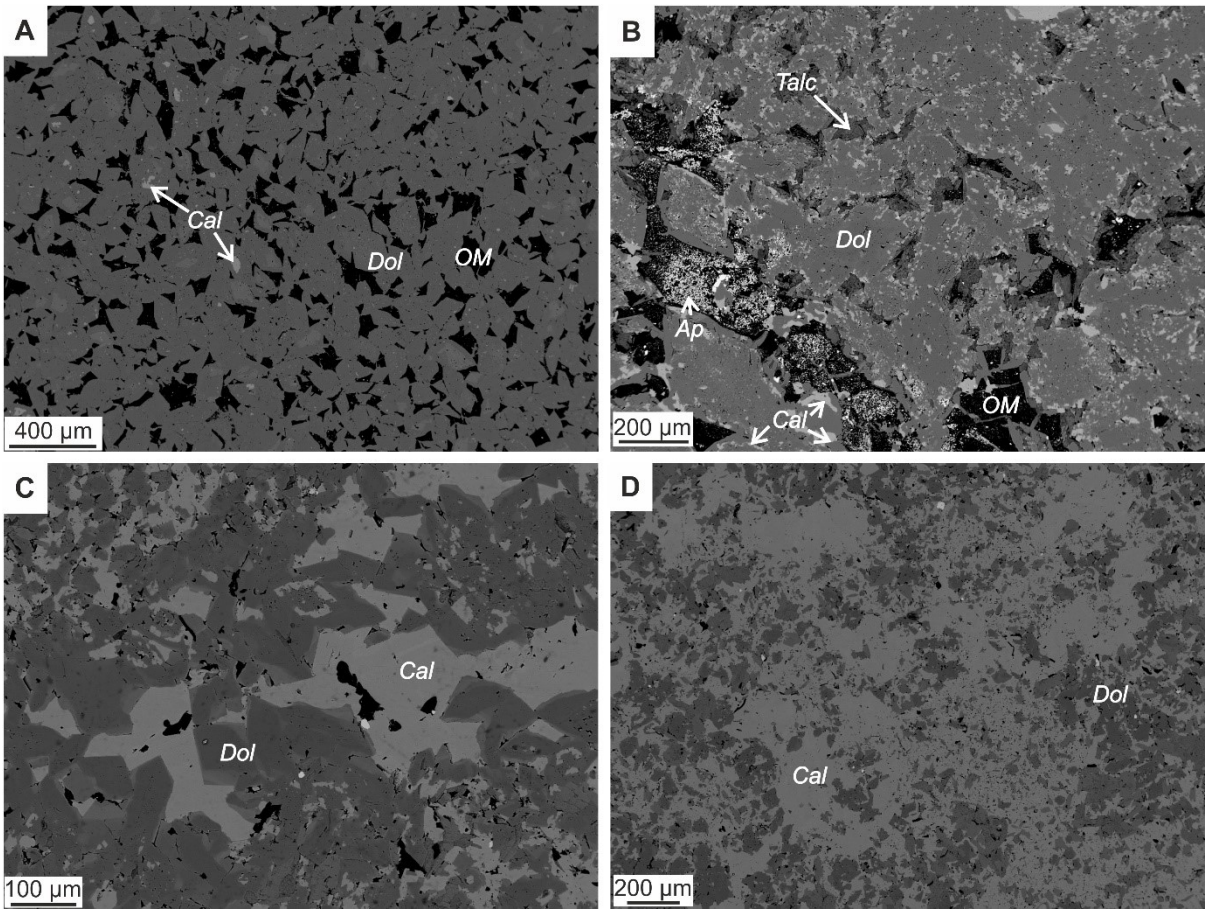

Figure 4. SEM images in BSD mode characterising carbonate rocks in Unit B. (A) Large planar-e dolomite crystals in an organic matrix; B1, depth 47.20 m. (B) Large planar-s dolomite crystals with abundant small calcite inclusions; B1, depth 50.77 m. (C) Secondary calcite and dolomite filling cavities. Slightly lighter areas in dolomite are more enriched in Fe compared to darker areas; B1, depth 52.92 m. (D) Massive dedolomitisation on the margin of the carbonate bed; B1, depth 52.92 m. Cal – calcite, Dol – dolomite, Py – pyrite, OM – organic matter.

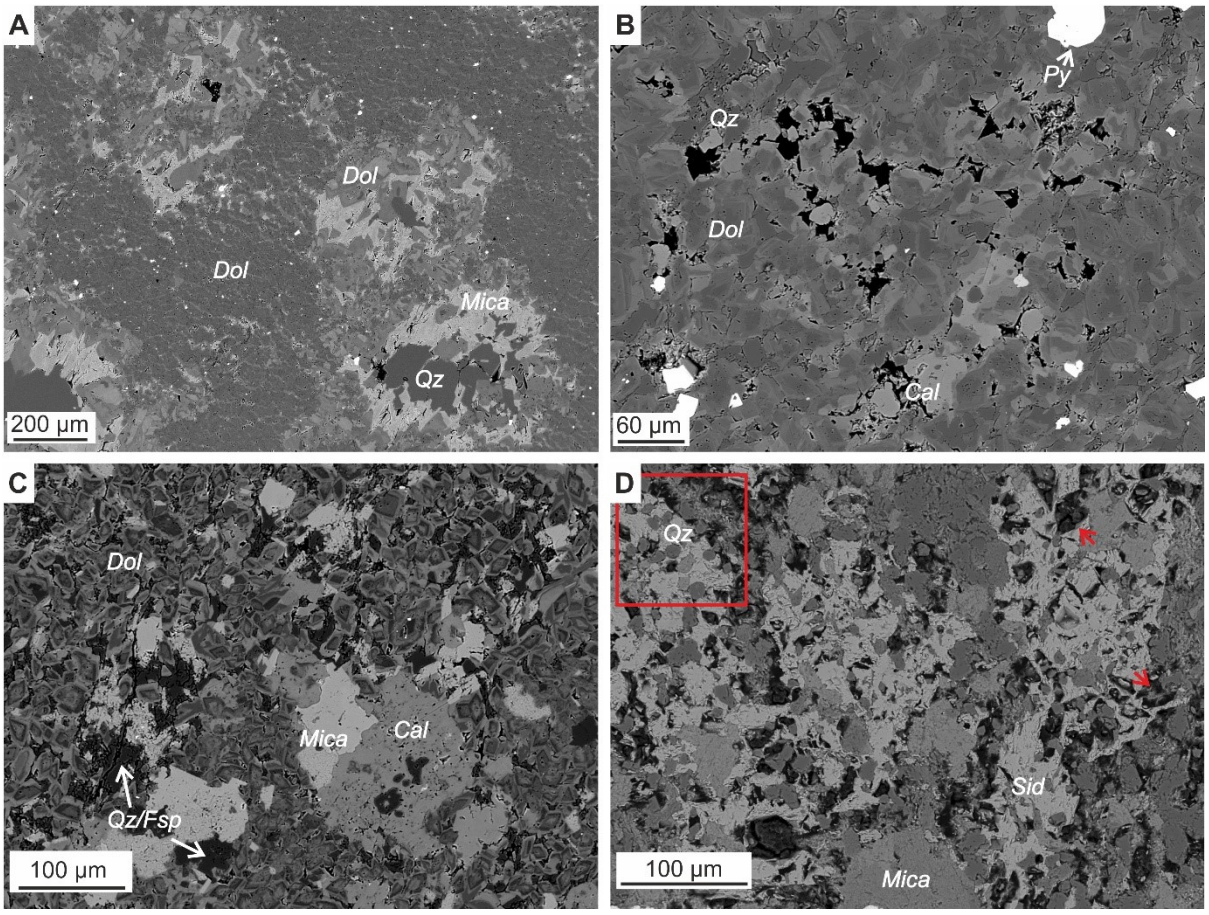

992

993 **Figure 5.** SEM images in BSD mode characterising carbonates in Unit C. (A) Small nonplanar
994 dolomite crystals with Fe-rich outer rims. Note larger secondary quartz-mica-dolomite
995 aggregates in which dolomite has varying concentrations of Fe; C1, depth 30.92 m. (B)
996 Moderately zoned dolomite crystals and secondary calcite with high porosity; C2, depth 29.28
997 m. (C) Small planar-e strongly zoned dolomite/ankerite crystals and a larger poikilitic calcite
998 aggregate; C2, depth 18.72 m. (D) Poikilitic siderite aggregates with abundant dissolution
999 marks (e.g., marked with red arrows). Note the well-rounded silt-sized quartz grains in the red
1000 square; C3, depth 6.5 m. Cal – calcite, Dol – dolomite, Py – pyrite, Qz – quartz, Fsp – feldspar,
1001 Sid – siderite.

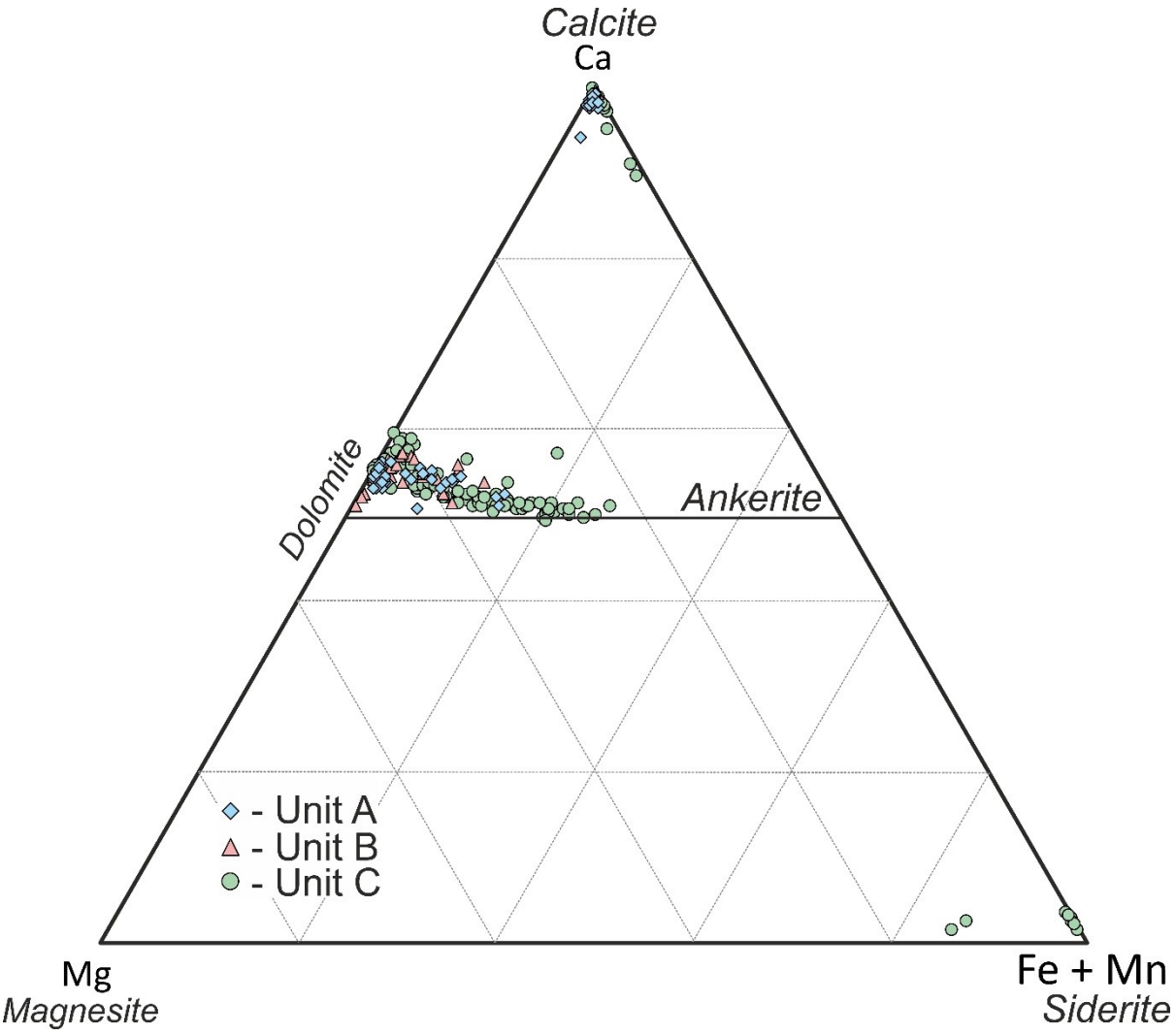

Figure 6. Major element composition (Ca, Mg, Fe, Mn) in mol% of carbonate minerals from the OnZap section measured with EDS. Siderite was found only in Unit C. Calcite and dolomite-ankerite were found in all units; however, dolomite in Unit C was closer to ankerite composition than dolomite from other units.

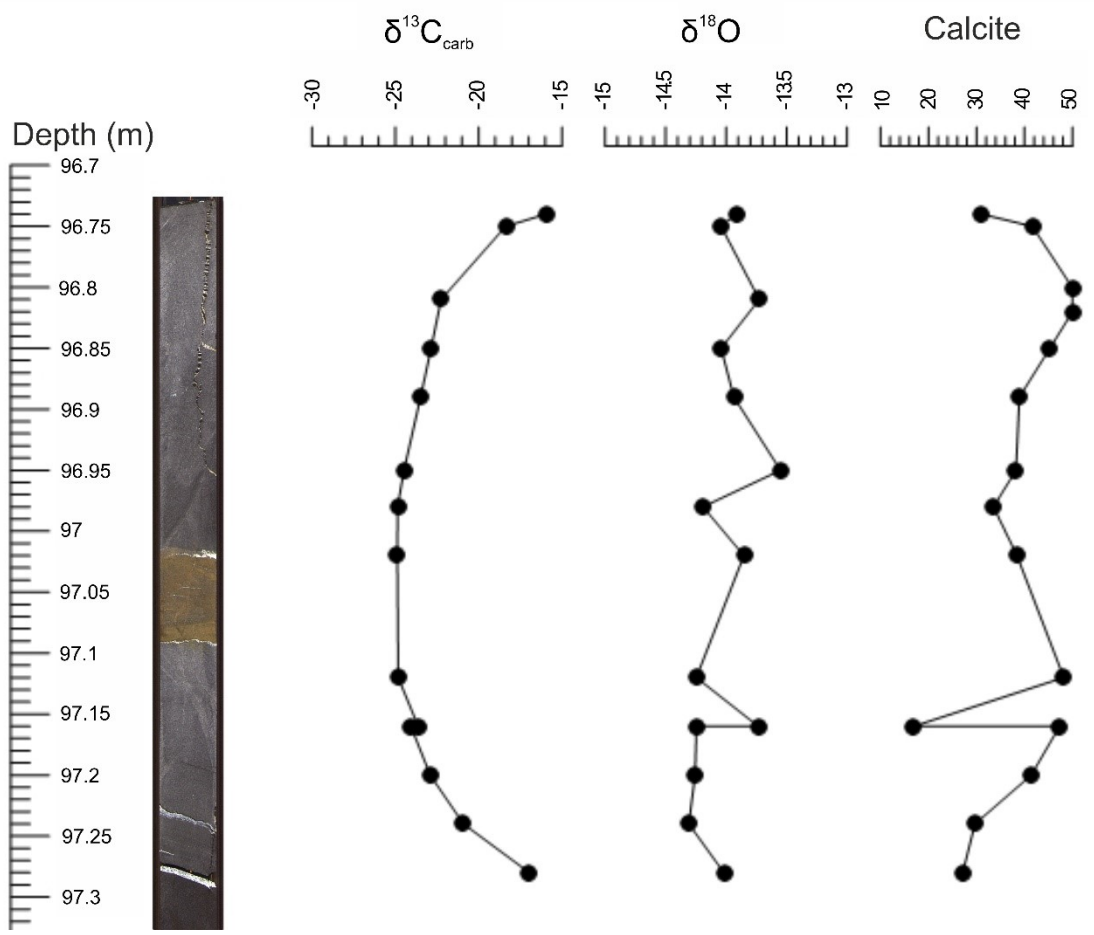

1008

1009 **Figure 7.** Carbonate $\delta^{18}O$ and $\delta^{13}C$ (‰, VPDB) and calcite abundance (wt.%) in the inferred

1010 methane derived carbonate interval A2 with primary calcite. The interior of the calcareous

1011 mudstone bed has lower $\delta^{13}C_{carb}$ values than the margins.

1012

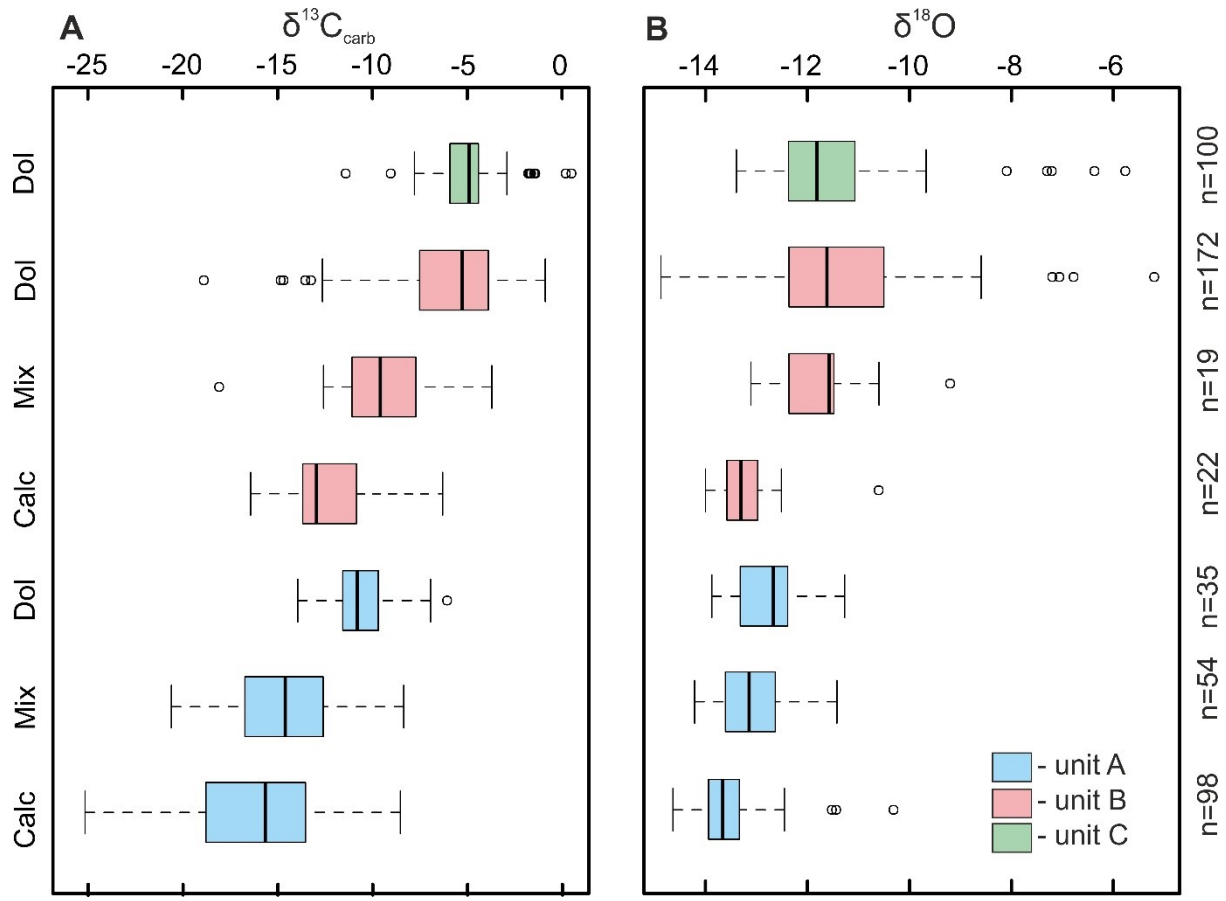

1013

1014 **Figure 8.** Box-plots with distribution of (A) $\delta^{13}C_{carb}$ (‰, VPDB) and (B) $\delta^{18}O$ (‰, VPDB)
1015 values in the OnZap section grouped by carbonate mineralogy. Note the general trend of
1016 increasing isotopic values from Unit A to C. Calcite-rich samples have systematically lower
1017 isotopic values than dolomite-rich samples. Unit C is mostly dolomitic and hence all data are
1018 grouped in one box. Calc – calcite wt.% to total carbonate wt.% >0.8; Mix – calcite wt.% to
1019 total carbonate wt.% = 0.8 – 0.2; Dol – calcite wt.% to total carbonate wt.% <0.2.

1020

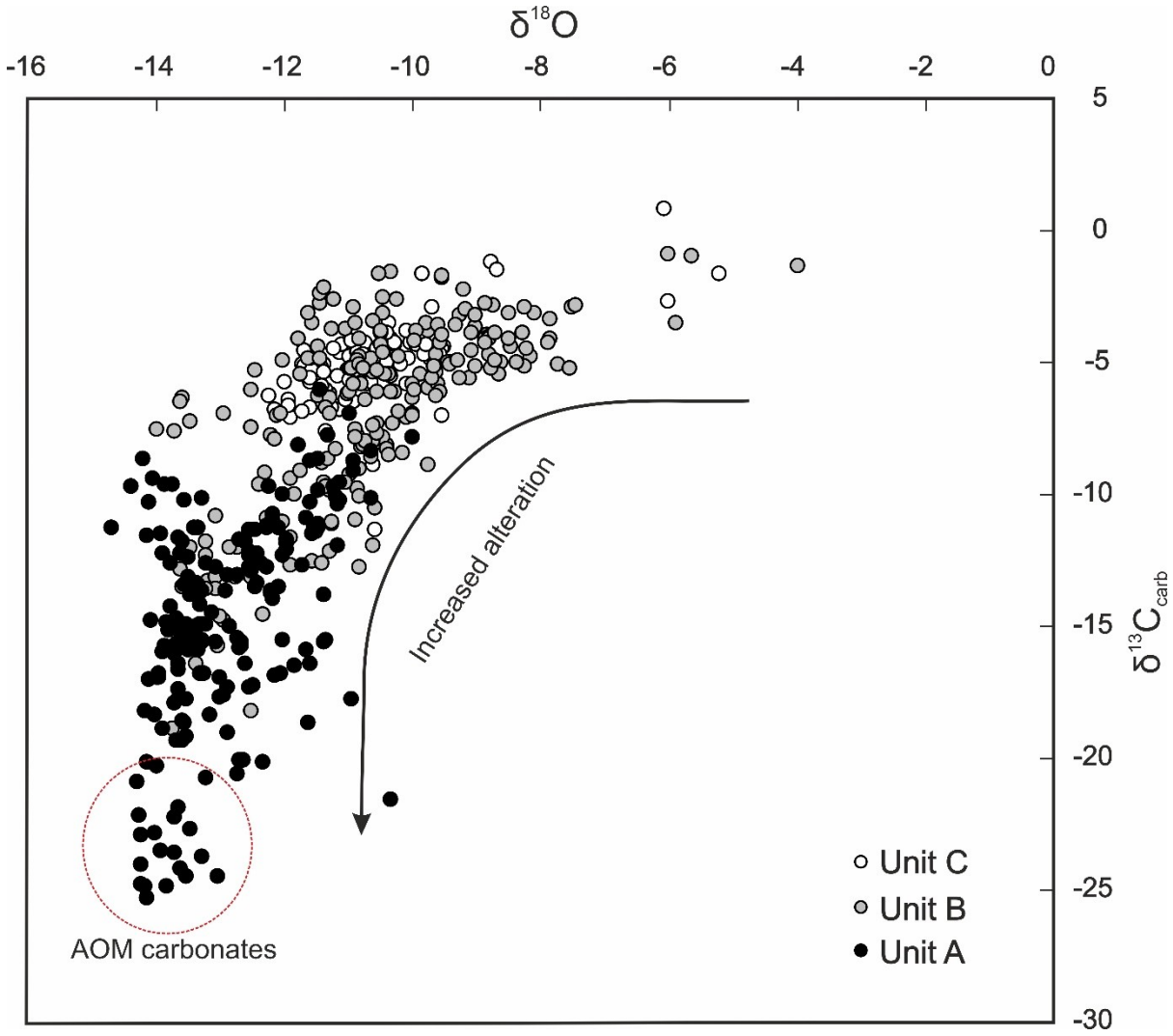

Figure 9. Cross-plot of $\delta^{13}C_{carb}$ and $\delta^{18}O$ (‰, VPDB) values from the OnZap section grouped by carbonate mineralogy. Note the L-shaped field, suggesting the complete resetting of the carbon and oxygen isotopic signal in some samples.

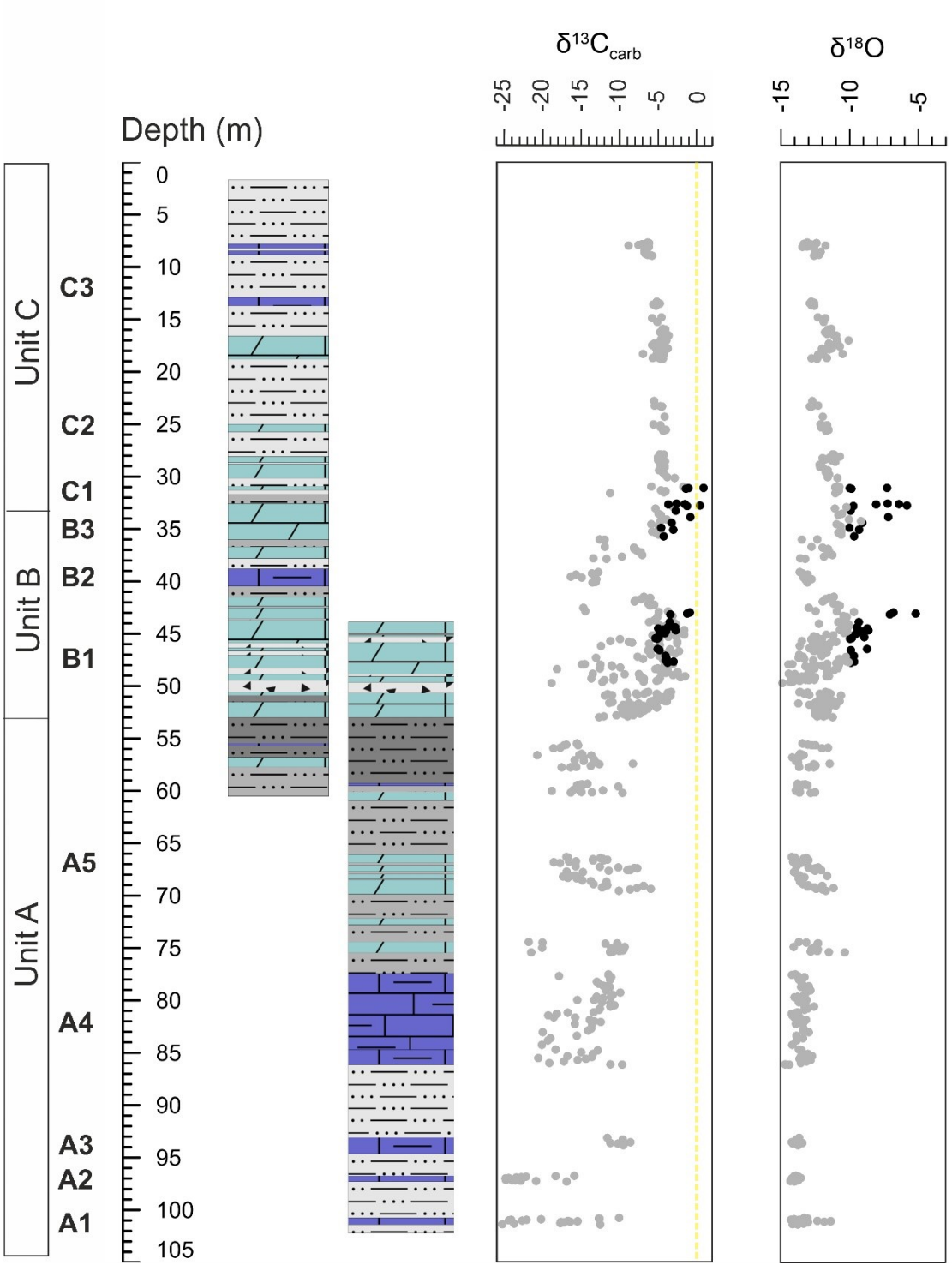

Figure 10. Screened (calcite to total carbonate ratio <0.05 and $\delta^{18}O$ values >-10.0‰) $\delta^{13}C_{carb}$ and $\delta^{18}O$ values (‰, VPDB) are marked as black dots and samples that did not pass the screening are marked as light grey dots. Lithological symbols as on Figure 2.

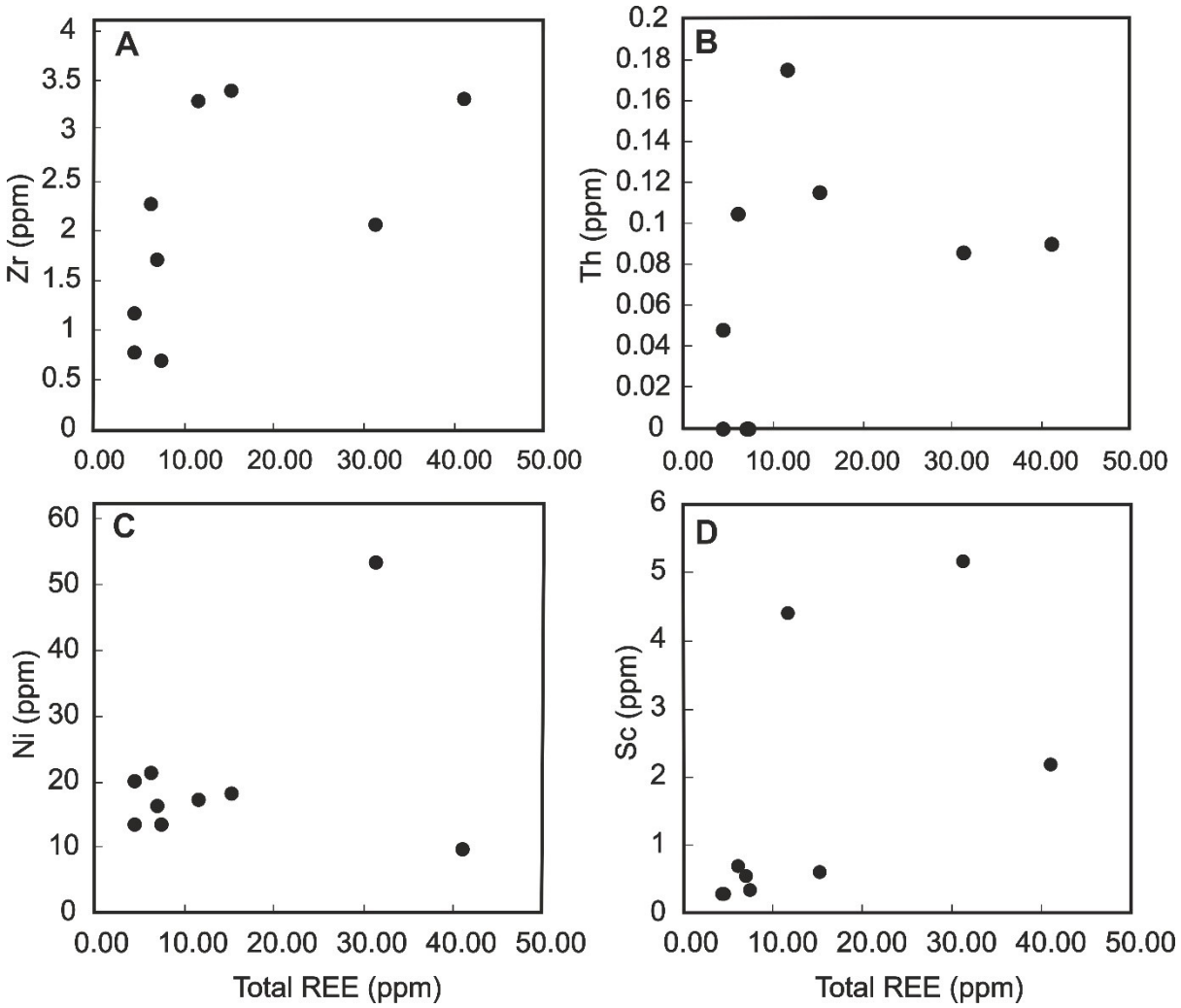

Figure 11. Element-total REE concentration plots of samples that passed screening for detrital REY contamination (i.e., Zr concentration <4 ppm). (A) Zr and (B) Th are used to evaluate siliciclastic, (C) Ni oxide and (D) Sc sulfide contamination. The absence of an obvious correlation between the element and total REE suggests no significant contamination.

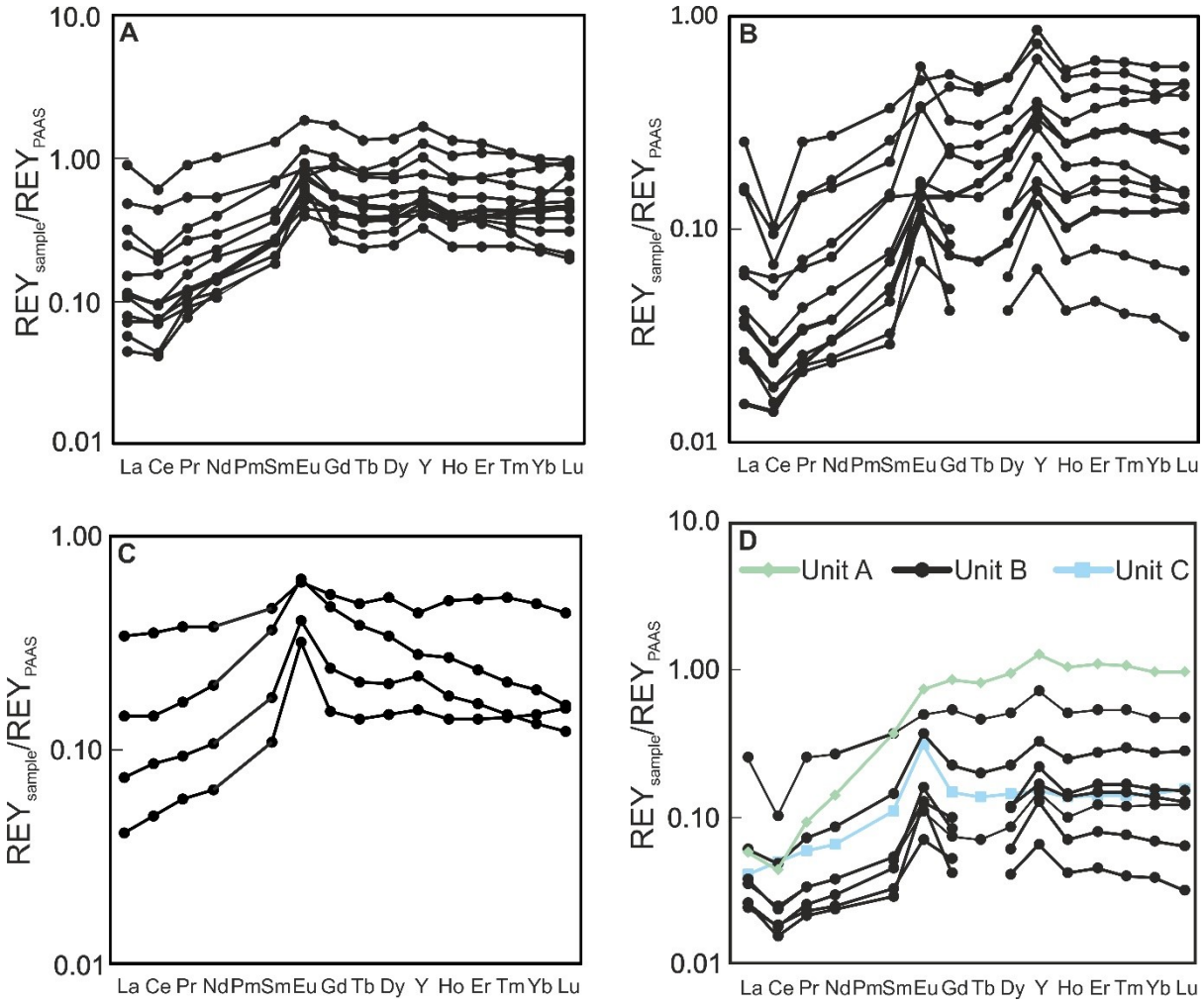

Figure 12. REY_{SN} patterns of Units A, B, C, and samples from all units (D) that passed screening (i.e., Zr <4 ppm). Unit A has a higher concentration of REY and shows MREE enrichment compared to LREE and HREE. Unit B has a coherent pattern but with varying REY concentration. Unit C is also enriched in MREE compared to other REE and does not show anomalous behaviour other than a positive Eu_{SN} anomaly. Samples from Unit A and C have a strong shale contamination and only one sample from each unit passed the screening.

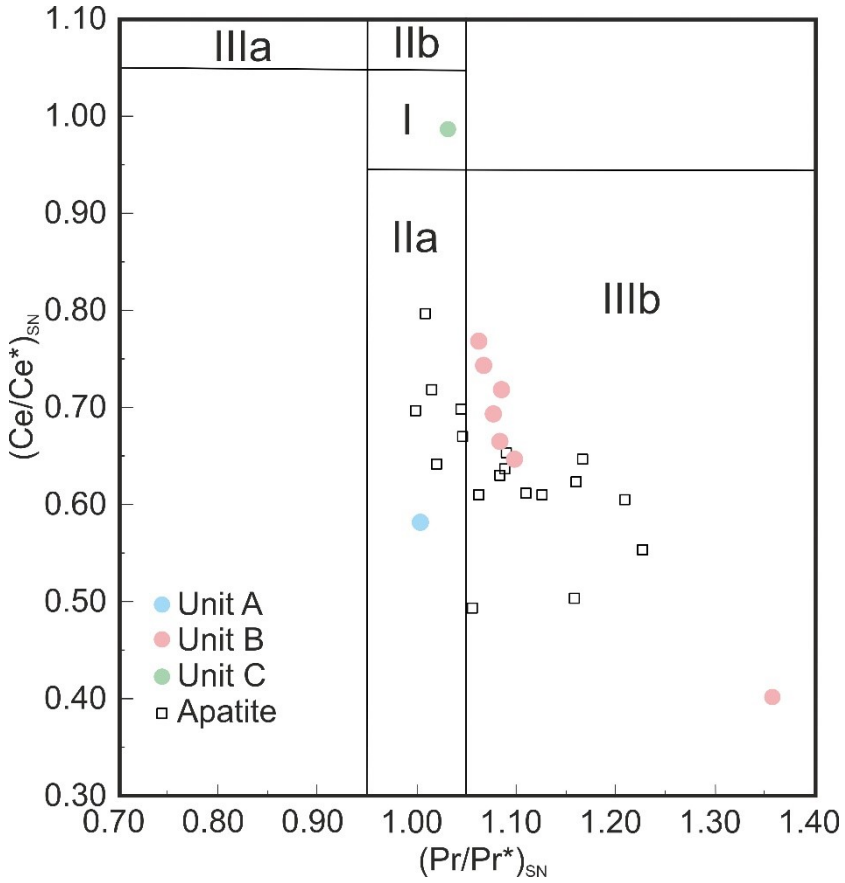

1044

1045 **Figure 13.** Plot of PAAS-normalised Ce/Ce* [Ce/(0.5La + 0.5Pr)$_{SN}$] vs Pr/Pr* [Pr/(0.5Ce +
1046 0.5Nd)$_{SN}$] for evaluating the Ce$_{SN}$ anomaly (after Bau and Dulski, 1996) in screened OnZap
1047 samples and diagenetic apatite data from Joosu et al. (2015) taken from the Shunga village
1048 outcrop that corresponds to B1 in the OnZap section. (I) no anomalous behaviour; (IIa) positive
1049 La$_{SN}$ anomaly, no Ce$_{SN}$ anomaly; (IIb) negative La$_{SN}$ anomaly, no Ce$_{SN}$ anomaly; (IIIa) positive
1050 Ce$_{SN}$ anomaly; (IIIb) real negative Ce$_{SN}$ anomaly. All of the screened samples from Unit B
1051 display a negative Ce$_{SN}$ anomaly, whereas the sample from Unit A plots in the positive La$_{SN}$
1052 anomaly field and that for Unit C shows no anomalous behaviour. Apatite REE data from the
1053 Shunga village displays similar but more varying patterns.

1054

1055

1056

Table captions

Table 1. Defined carbonate bed intervals with the average carbonate mineralogy and isotopic values. B.d. stands for below detection (<0.5 wt.%).

Supplementary table captions

Supplementary Table 1. Mineralogical composition (wt.%), $\delta^{13}C_{carb}$ (‰, VPDB) and $\delta^{18}O$ (‰, VPDB) values ±0.2‰ (2σ) of the OnZap section. Tr <0.5 wt.%.

Supplementary Table 2. Major and trace element concentration in the OnZap section. Ca, Mg, Fe and Mn in wt.% and trace elements in ppm.

Supplementary Table 3. REY systematics of the OnZap section. Samples that did not pass screening are in italics